The Mechanism of Thin Film Si Nanomachining Using Femtosecond Laser Pulses

by

Jimmy Yi-Jie Jia

Submitted to the Department of Material Science and Engineering
in partial fulfillment of the requirements for the degree of

Masters of Science in Material Science and Engineering

at the

MASSACHUSETTS INSTITUTE OF TECHNOLOGY

June 2004

© Massachusetts Institute of Technology 2004. All rights reserved.

Author ....
Department of Material Science and Engineering
April 22, 2004

Certified by ....
Carl V. Thompson II
Stavros Salapatas Professor of Materials Science and Engineering
Thesis Supervisor

Accepted by ....
Carl V. Thompson II
Stavros Salapatas Professor of Materials Science and Engineering
Chair, Departmental Committee on Graduate Students

The Mechanism of Thin Film Si Nanomachining Using Femtosecond Laser Pulses

by

Jimmy Yi-Jie Jia

Submitted to the Department of Material Science and Engineering
on April 22, 2004, in partial fulfillment of the
requirements for the degree of
Masters of Science in Material Science and Engineering

Abstract

Femtosecond (fs) laser ablation has been the subject of intense recent research. The pulse time ('width') is shorter than the electronic relaxation time, resulting in a decoupling of the period of laser illumination and the melting of the substrate. Since the laser does not directly heat the substrate, and there has been no directly observed heat affected zone (HAZ) nor vaporization, fs laser ablation is sometimes considered to be a direct solid-vapor phenomenon.

Recent research indicates that the phenomenon is not as straightforward as assumed. Time-of-flight spectroscopy used to measure the reflectivity indicates that molten material is present for a few hundred picoseconds, well after the laser pulse. A material-modification threshold has been observed that is below the ablation threshold. This indicates that the laser can affect the substrate without ablation occurring. However, many scanning electron microscopy (SEM) studies have been performed, but material change in the substrate have not been observed. Transmission electron microscope (TEM) studies have also been done, but they have all been carried out in plane-view, so that it is difficult to separately observe bulk and surface effects.

In this study, cross-sectional TEM analysis of holes drilled in single crystal silicon films in silicon-on-insulator (SOI) structures have been carried out, and have allowed direct observation of the subsurface modified material. Samples were prepared using a focused ion beam (FIB) system, and a metal mask was applied to protect the surface from the ion beam. Through transmission electron microscopy, electron diffraction analysis and energy dispersive x-ray (EDX) analysis, a surface layer of clearly modified material was identified as amorphous silicon (a-Si). This demonstrates that conventional heating of adjacent material occurs during femtosecond pulsed laser ablation. Furthermore, cross sectional transmission electron microscopy allows direct measurement of the extent of the heat-affected zone.

Secondary effects were also observed in the SOI structures. An a-Si layer was observed below the insulator (SiO_2) layer, indicating that the SiO_2 is transparent to the laser beam and that the a-Si formed without ablation or recondensation. There was also undercutting of the top layer of silicon as well as the formation of bubble in the oxide layer. These

observations also provide evidence for the nature and extent of heating that occurs during femtosecond pulsed laser ablation.

Thesis Supervisor: Carl V. Thompson II
Title: Stavros Salapatas Professor of Materials Science and Engineering

Acknowledgments

There are many people whose time and dedication went into writing this thesis. First and foremost are my parents who have given me the opportunity to pursue this degree.

Next is Professor Carl Thompson for his inspiration and guidance. I would also like to thank Dr. Ming Li of Panasonic Technologies for his support and advice, both technical and otherwise, throughout the duration of the project.

I would like to thank Makoto Ishizuka, Daniel Hogan, Xinbing Liu, and Kiyotaka Mori of Panasonic Technologies for their useful discussions and suggestion along the way.

I would like to thank Warren Moberly-Chan of Harvard University for his assistance on the FIB and help in perfecting the technique. In addition, his aid in taking the TEM micrographs has been invaluable.

I would also like to thank Kurt Broderick and the rest of the staff of the Microsystems Technology Laboratories for their dedicated technical assistance.

I would also like to thank Andrew Takahashi for his help in the thermal calculations and the rest of the Thompson group for their suggestions.

Finally, I would like to thank all of my friends, who read proofs of this work, and who have kept me (relatively) sane(er) in the last many years.

This work was performed under the Femtosecond Technology Research Association (FESTA), which is supported by the New Energy and Industrial Technology Development Organization (NEDO).

Contents

1 Introduction **15**

2 Literature Survey **19**

2.1 Introduction 19

2.2 Nanosecond Laser Ablation Mechanism 19

2.3 Femtosecond Laser Ablation Thresholds 20

2.4 Advantages of Femtosecond Laser Ablation 24

2.5 Ablation Mechanism for the Femtosecond Regime 25

3 Experiments **29**

3.1 Introduction 29

3.2 Laser Setup 29

3.3 Drilling Parameters 31

3.4 TEM Sample Preparation 32

3.5 Analytical Tools 33

4 Results **37**

4.1 Introduction 37

4.2 SEM results 37

4.3 TEM Results 38

4.4 Evolution with Increasing Number of Pulses 47

5 Discussion **57**

5.1 Introduction 57

5.2 Amorphization 57

5.3 Calculations 58

5.4 Length Scales 61

5.5 Secondary Effects 62

6 Conclusions and Future Work **65**

A Measurement of Laser Parameters **67**

A.1 Introduction 67

A.2 Laser Spot Size 67

A.3 Intensity of the Laser Beam 69

A.4 Focal Depth 70

A.5 Finding the Focus Distance of the Laser Beam 71

B TEM Sample Preparation **73**

B.1 Coating with Metal 73

B.2 Die-Saw Technique 74

B.3 FIB Technique 76

List of Figures

1-1 SEM image of holes drilled using a femtosecond laser beam. We see a fully ablated region (∼200 nm dark hole) and a surface modified region (∼600 nm light region) around each fully ablated hole. 17

2-1 The drilling of a steel film using nanosecond, picosecond, and femtosecond pulses. Each hole is slightly over 100 μm. Notice that the drilling by the fs laser is the cleanest [3]. 21

2-2 This demonstrates the wavelength dependence of the ablation threshold for two dielectrics. The squares points are for $\lambda = 800$ nm and the circle points are for $\lambda = 400$ nm. The unfilled points are calculated from theory. Figure taken from [13]. 23

2-3 A schematic diagram of sub-micron drilling. Only the portion of the laser beam that is above the ablation threshold will remove material from the substrate [1]. 24

2-4 Calculated temperatures for the surface of a titanium sample at two laser fluences. Notice the delay in rise of lattice temperature [7]. 27

3-1 Schematic of the laser setup [4]. 30

3-2 Layout of the drilled holes. There is a 3×5 alignment mark and a row of holes with increasing number of pulses. 32

3-3 A before-and-after schematic diagram of the processing of the samples. The goal is to create profiles of the holes for TEM analysis. 34

3-4 Before-and-after SEM micrograph of drilled sample. (A) SEM top view of holes (B) SEM profile after FIB milling. Note the profiles of the holes are visible. 34

4-1 Particles splattered ∼2μm diameter around the 3 × 5 alignment holes. . . . 39

4-2 High magnification of one of the alignment holes. Particles < 100 nm in diameter are scattered around a 500-pulsed hole. 39

4-3 Fewer particles are found around the alignment holes when 20 psi of argon is blown over the surface during drilling. 40

4-4 High magnification of a 500-pulsed hole with 20 psi of argon blown during drilling. Particles are now < 20 nm in diameter. 40

4-5 SEM micrograph of drilled holes with various numbers of pulses. 41

4-6 SEM micrograph of drilled holes with various numbers of pulses, cont. 42

4-7 SEM micrograph of drilled holes with various numbers of pulses, cont. 43

4-8 Measurements of the diameter of the heat affected zone and the ablated hole vs. number of pulses as measured from the SEM micrographs. 44

4-9 A TEM micrograph of a region unmodified by the laser beam. (A) Top layer of Cr, (B) Pt, (C) Cr adhesion layer, (D) silicon native oxide, (E) top layer Si, (F), buried oxide, and (G) bulk silicon. 45

4-10 Cross-section TEM Micrograph of a five-pulsed hole. (A) Top layer of Cr, (B) Pt, (C) Cr adhesion layer, (D) silicon native oxide, (E) top layer Si, (F) buried oxide, (G) bulk silicon, and (H) laser modified layer. 45

4-11 EDX spectrum of the modified region (H) in Fig. 4-10. Note the large Si peak 46

4-12 EDX of the buried oxide, layer (F) in Fig. 4-10. There is a substantial oxide peak. 46

4-13 Cross-sectional TEM of a 25-pulsed hole where the top surface is completely ablated. (A) is taken on the zone axis. (B) is taken on the <110> plane. . . 48

4-14 TEM cross-sectional micrographs of holes ablated for various numbers of pulses. 51

4-15 TEM cross-sectional micrographs of holes ablated for various number of pulses, cont. 52
4-16 TEM cross-sectional micrographs of holes ablated for various number of pulses, cont. 53
4-17 Diameters of holes from the TEM micrographs. They are measured at the top, middle and bottom of the top layer Si (layer (E) of Fig. 4-10). Note the diameter of near the interface of the bulk Si/SiO_2 is larger than the diameter of the middle. 54
4-18 Diameter of the modified region in the bulk silicon. 54
4-19 TEM micrograph of the modified area in the bulk silicon under the oxide after 60 pulses. (A) is recrystallized into the oxide (see Fig. 4-20) (B) is a polycrystalline region (see Fig. 4-21) (C) is crystalline material in the bubble (see Fig. 4-22). 55
4-20 Region (A) in Fig. 4-19. Tip of the modified region that protrudes into the oxide. We can see lattice fringes indicating crystalline features in the oxide. . . 55
4-21 Region (B) in Fig. 4-19. Lattice fringes for polycrystalline material under the oxide. 56
4-22 Region (C) in Fig. 4-19. Lattice fringes indicating crystalline material in the bubble. 56

5-1 The FD of the laser can spread into the bulk silicon. This may cause the melting of the bulk material. 63
5-2 If the laser is focused too high, undercutting may occur due to the spread of the laser beam. 64

A-1 A schematic diagram of the last two lenses in the laser setup. 68
A-2 An array of holes made to find the focus point. The row with the best holes represented the optimal focal distance. 72

B-1 Drilled area and the cross hair. 74

B-2 FIB milled edge of a sample masked with Cr. Note the well defined edge. . . 75
B-3 FIB milled edge of a Platinum masked sample. Note the large overspray due to the ion beam. 75
B-4 Note the good edge and protection with a sandwich mask of Cr/Pt/Cr. . . . 76
B-5 Optical microscope picture of a 300 μm wide sliver. 77
B-6 After a 20 kpA rough milling in the FIB 78
B-7 After the 2nd milling with a 3 kpA beam 78
B-8 After 100 pA fine milling. 79
B-9 Top view of the milled sample. Note the three rows of alignment holes on the right. The middle row is the row with the drilled samples. 79

List of Tables

2.1 Comparison of the single shot ablation threshold for dielectrics, metals, and semiconductors. 22

Chapter 1

Introduction

Laser machining has had a significant impact in many fields in the last thirty years. Laser cutting and milling techniques are more accurate than their mechanical counterparts. Laser ablation mechanisms are also material independent, making them suitable for the manufacturing of a wide range of products. They have been used from the manufacture of aircraft turbine blades, to the machining of delicate medical tools, to the cleaning of archaeological finds.

The peak intensity of the power can be increased dramatically by shortening the pulse of the laser beam. Since power is measured in joules per second, power can be increased by increasing the energy or by shortening the pulse. Ultra-short laser pulses, picosecond (ps) and femtosecond (fs) lasers, make it possible to achieve very high peak intensities with low pulse energies. For instance, a laser pulse with a width of 100 fs and energy of 0.33 J has a peak intensity of 10^{15} W/cm^2 when focused onto a 20 μm spot. A 10-nanosecond (ns) long laser pulse would have to have to be 100 J to reach the same intensity [1].

The mechanism for the removal of material changes as the pulse width decreases. For lasers with nanosecond and longer pulses, the removal of material is a thermal damage process. The laser spot heats the surface and some heat is conducted to the material surrounding the spot, melting the sample. Some material is vaporized, and the resulting vapor pressure can reach many hundreds of GPa's [2]. Material is removed by melt expulsion due to the

intense vapor pressure. Because of the thermal nature of the process, a large volume of material is heated and melted. In the fs regime, laser-matter interactions are decoupled from the removal of material. The pulse width is too short for heat to diffuse from the area of focus, limiting the deposited energy within a shallow layer of the material surface. The highly concentrated energy heats the substrate to the vapor phase and the material is vaporized from the surface. Because of this, fs laser ablation is said to have a direct solid-vapor transition [3].

In the machining of photonic waveguides [4], sub-micron features are drilled using an fs laser in a piece of silicon that is 1 μm wide. Figure 1-1 is a photonic waveguide that is 1 μm wide with holes that are $\sim$400 nm across. Around each of the holes is a $\sim$800 nm modified area that did not ablate. The direct solid-vapor model does not take into account the modification to the surface, indicating that there is more to the ablation than previously suggested.

The goal of this thesis is to characterize the modified area around an ablated hole and to shed light on the mechanism of fs laser ablation. Single and multiple shot ablated holes were drilled silicon-on-insulator (SOI) samples. Cross-sectional transmission electron microscope (TEM) analysis was performed on the drilled samples. This allowed for direct observation and identification of the modified layer.

Chapter 2 of the thesis will give a literature review of laser technology and mechanisms for ns and fs ablation. Chapter 3 will outline the experimental procedures. In Chapter 4, we will present the results and discuss them in Chapter 5. Finally, in Chapter 6, we will draw our conclusions and give some ideas for futures work in this field.

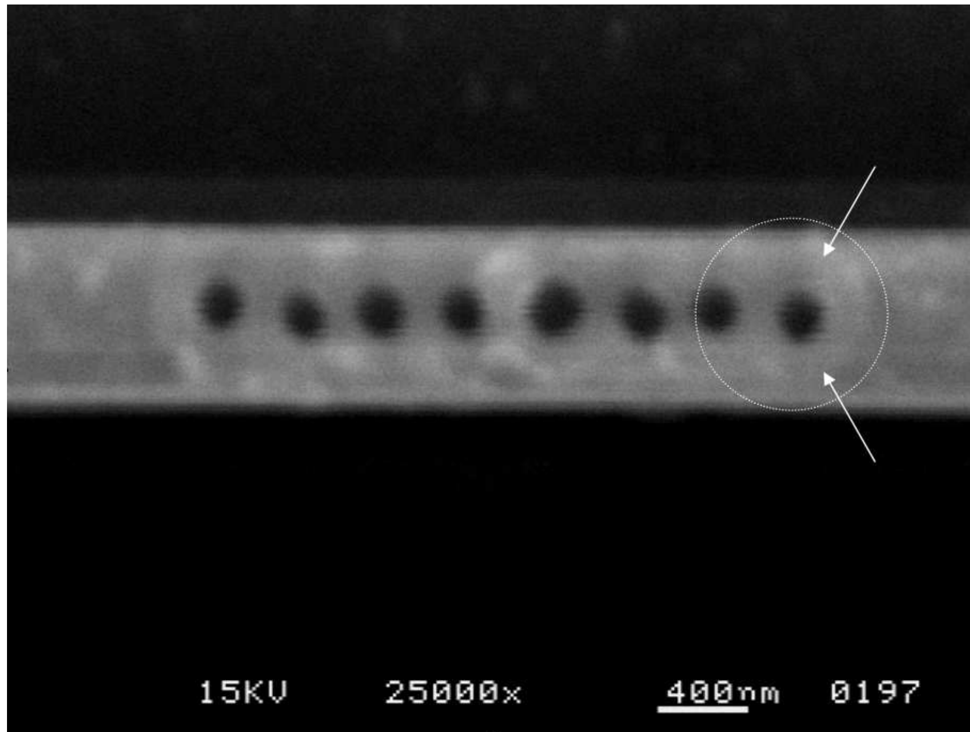

Figure 1-1: SEM image of holes drilled using a femtosecond laser beam. We see a fully ablated region (∼200 nm dark hole) and a surface modified region (∼600 nm light region) around each fully ablated hole.

Chapter 2

Literature Survey

2.1 Introduction

This chapter will give a brief background in laser technologies. We start with a introduction on the mechanism for nanosecond ablation. We will then discuss the differences between long pulsed and short-pulsed laser ablation. After that, we will review some of the work done on femtosecond ablation, including a discussion on ablation thresholds. Finally, we will provide a review of the existing theories on femtosecond laser ablation.

2.2 Nanosecond Laser Ablation Mechanism

Generally, laser pulses in the nanosecond (ns) range are considered to be short pulsed while the picosecond (ps) and femtosecond (fs) regime are considered to be ultra-short pulsed. The ablation mechanism by continuous wave (cw) and short-pulsed lasers is a thermal process that involves direct vaporization. The laser beam deposits energy in a shallow layer close to the surface. The surface reaches thermal equilibrium and some of the heat conducts to the material surrounding the laser spot. A molten layer forms and continuous application of the laser vaporizes the substrate. Material is removed by melt expulsion aided by a locally high vapor pressure. The material splatters around the irradiated area and solidifies as residue

in the surrounding area [5]. The thermal effects have created an observed 40 μm thick heat affected zone (HAZ) in aluminum [6]. Strong shock waves generated by the explosive change of phase can cause mechanical stresses in the material [7]. The formation of liquid and vapor phases around the spot interfere with the precision of the laser machining [3] by deflecting the beam. Laser machining with ns laser pulses results in a large heat affected area and creates a large splatter zone for expulsed material.

In the picosecond regime, a melted zone also forms around the target. The presence of the liquid interferes with the precision of the laser machining [3], but there is a vast improvement over the results in the nanosecond regime. In the femtosecond regime, there is virtually no interaction between the laser beam and the excited electrons which provides for a very clean and precise cut. Heating and cooling happens well after the application of the laser beam, thus decoupling substrate heating with the laser illumination. Figure 2-1 shows a sequence of laser holes created using nanosecond, picosecond and femtosecond pulses. Clearly, as the pulse width decreases, the precision of the ablation increases, resulting in a cleaner cut.

2.3 Femtosecond Laser Ablation Thresholds

Ablation occurs only if the laser fluence, or energy per unit area, is above a certain threshold, Φ_{TH}. At fluences significantly above the ablation threshold, surface temperatures are high, material is ejected, and pits are formed. The ejected material solidifies as amorphous or crystalline solids. At fluences below the ablation threshold, surface temperatures are lower, and the material does not have enough time to re-crystallize from the melt.

Much work has been done to determine the threshold. The ablation threshold is determined by measuring the diameter of the hole versus the pulse fluence and extrapolating to zero [8, 9]. The value for the threshold depends on many variables, namely, the pulse width, the material, the number of pulses, and the wavelength.

Table 2.1 compares Φ_{TH} for a range of materials, from dielectrics to metals to semiconductors. As one can see, the threshold values are within a small fluence range, even between ultra-hard dielectrics, such as CaF_2 and relatively soft metals, such as Cu. This is

ns

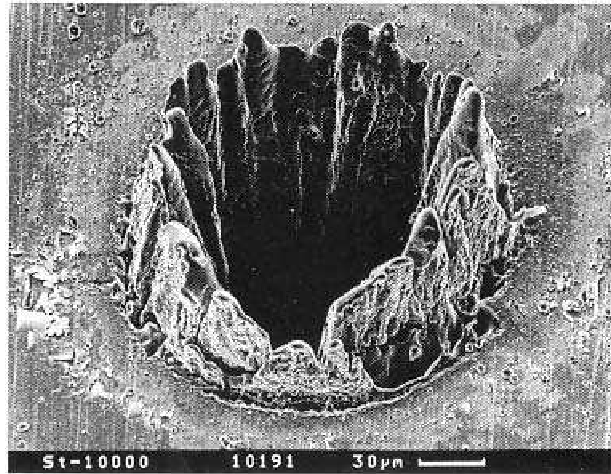

ps

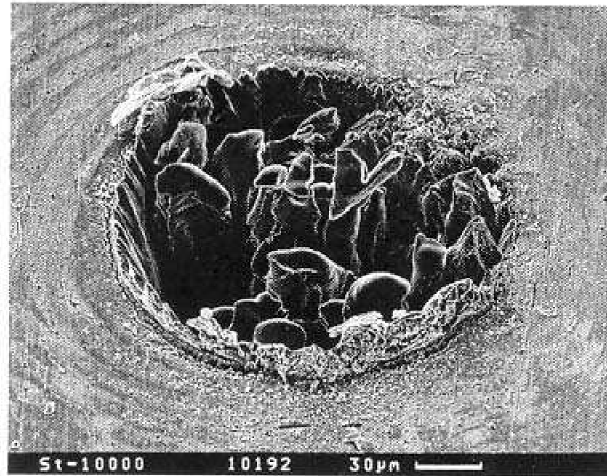

fs

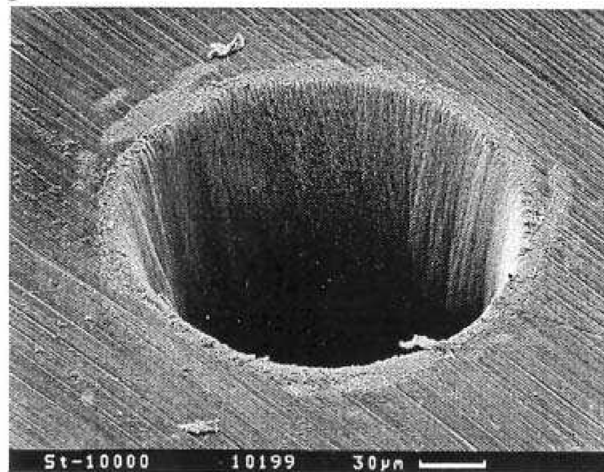

Figure 2-1: The drilling of a steel film using nanosecond, picosecond, and femtosecond pulses. Each hole is slightly over 100 μm. Notice that the drilling by the fs laser is the cleanest [3].

Table 2.1: Comparison of the single shot ablation threshold for dielectrics, metals, and semiconductors.

Material	Pulse Width (fs)	Wavelength (nm)	Φ_{TH} (J/cm^2)
Fused Silica[13]	40	800	1.3
CaF_2 [13]	40	800	1.0
C (Diamond) [15]	100	800	1.3
TiN [15]	100	800	0.03
Al [5]	150	400	0.6
Cu [5]	150	400	0.72
Pt [5]	150	400	1.20
InP[14]	130	800	1.3

advantageous because the fs laser beam can ablate a wide range of materials. Regardless of how accurately the threshold is determined, it is difficult to stabilize the fluence of the laser during processing. Fluctuations of laser energies can commonly run up to 50% [9].

There is a strong dependence of the ablation threshold on the incident wavelength. At $\lambda = 620$ nm, the band gap is exceeded by over 1 eV. At $\lambda = 258$ nm, the band gap is exceeded by over 3 eV. By using a shorter wavelength laser, the threshold for ablation is reduced. This can be seen in reference [13] where the ablation thresholds were calculated for silica and CaF_2. At a shorter wavelength, the threshold for ablation is lower. The data is reproduced here in Figure 2-2. In both materials, the threshold fluence for ablation decreases by decreasing the wavelength. In <100> silicon, the single-shot ablation threshold in the femtosecond regime has been reported to be 0.1 J/cm^2 at $\lambda = 620$ nm [10], and 0.2 J/cm^2 at $\lambda = 780$ nm [9, 12].

The ablation threshold also depends on the number of pulses being applied [9]. If the fluence is below the one-shot ablation threshold, it is still possible to ablate the material by increasing the number of pulses. Ablation may occur even if the fluence is below the modification threshold. This seems to indicate the presence of an incubation effect that follows the power law

$$\Phi_{TH}(N) = \Phi_{TH}(1)N^{\zeta-1}[14]. \tag{2.1}$$

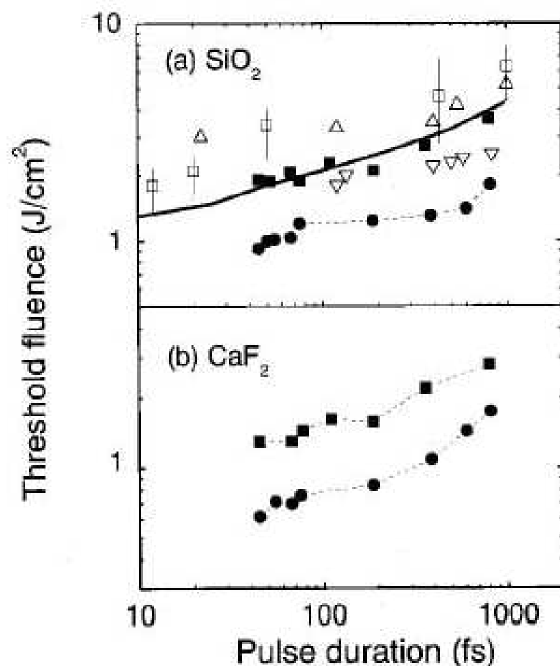

Figure 2-2: This demonstrates the wavelength dependence of the ablation threshold for two dielectrics. The squares points are for $\lambda = 800$ nm and the circle points are for $\lambda = 400$ nm. The unfilled points are calculated from theory. Figure taken from [13].

It is known that the incubation effect is not the result of a thermal memory due to the application of the laser beam [16]. The mechanism for the incubation mechanism is not well understood, and much work is being done to understand it [14].

It is also known that the orientation of the silicon substrate will affect the ablation threshold. Amorphization occurs more readily within 15° of the <111> plane in Si [22]. This indicates that less energy would have been needed to amorphize material on the <111> plane. A lower energy for amorphization implies a lower ablation threshold.

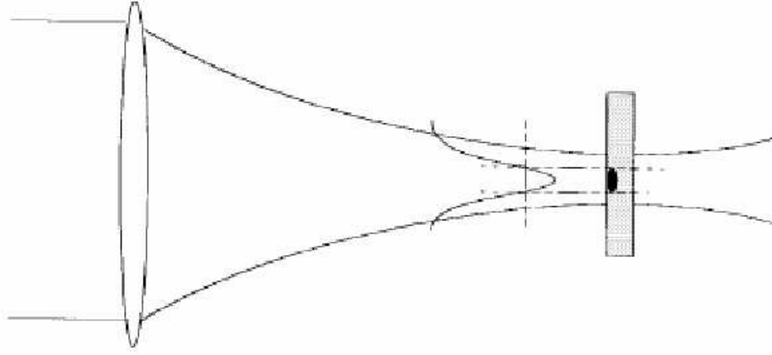

Figure 2-3: A schematic diagram of sub-micron drilling. Only the portion of the laser beam that is above the ablation threshold will remove material from the substrate [1].

2.4 Advantages of Femtosecond Laser Ablation

From the preceding section, it follows that there are several advantages in going to shorter pulse width. First, by decreasing the pulse width, the heat affected zone is decreased due to less heat loss. The laser beam does not directly heat the substrate and the thermal effects are limited to the laser spot size. Second, it is possible to avoid interactions of the laser beam and the plasma formed during laser ablation. This allows for cleaner and finer cuts. Finally, once Φ_{TH} is established for a set of parameters, ablation will occur only above that threshold.

It is possible to take advantage of the well-defined fluence threshold to drill features smaller than the spot size of the laser beam [12]. Since the laser beam is Gaussian in nature, it is possible to set the laser profile such that only the tip of the beam is above the ablation threshold. In this case, only the tip of the laser beam will ablate the substrate. Figure 2-3 is a schematic diagram of the effect. Using this technique, it has been shown that it is possible to machine features ∼200 nm in size using a ∼600 nm beam, as shown in the holes of Figure 1-1.

2.5 Ablation Mechanism for the Femtosecond Regime

For ultrashort lasers, the pulse width is too short for the heat to be conducted away from the surface during illumination. In the femtosecond regime, the laser beam deposits its energy into the surface of the material, excites electrons to the conduction band and generates an excess of electrons. The laser pulse duration is shorter than the electron relaxation time, which is on the order of picoseconds. By the time the laser beam is turned off, the system is out of equilibrium as the electrons are at a much higher temperature than the ions [1]. In this case, absorption of the laser and heating of the electrons in the surface layer, diffusion of 'hot' electrons into the bulk of the material, and energy exchange between the electron and phonon sub-system happen nearly simultaneously. It has been postulated that the highly concentrated energy heats the material quickly past the melting phase to the vapor phase. Since the heat does not have time to diffuse, the heat affected zone is greatly reduced. The depth of the optical absorption determines the thickness of the heated layer and is independent of the pulse duration [17].

This indicates that ablation occurs via a direct solid-vapor transition. The timescale for ablation is sufficiently short to ignore all thermal effects, to the first order [3], and all hydrodynamic motion [1]. One indication of this phenomenon is the absence of an observable heat affected zone. In Figure 2-1, the femtosecond laser gives the cleanest cut with no visible collateral damage. Harzic et al. did not observe a heat affected zone in fs ablation of Al, but concluded that the heat affected zone was smaller than their observational limit of 2 μm [6].

Another theory is that heating can occur electronically via fast Auger recombination. The presence of amorphous silicon (a-Si) in certain experiments indicates rapid thermal effects because a-Si forms from the rapid cooling of liquid silicon (l-Si) [18]. In the nanosecond timescale, where thermal melting occurs, melt expulsion by vapor pressure "pushes" molten material above the surface, leaving behind an amorphous ring [12]. This process was observed for the picosecond timescale as well when amorphous rings were seen to form around an ablated hole [18]. Ablation would occur by a homogeneous nucleation of gas bubbles at the surface causing an explosion and expelling of material [2, 19]. This would indicate that even

though the laser beam is not directly heating the substrate, the ablation process can be explained using traditional thermal models.

Third, the mechanism may be delayed Auger recombination [10]. Here, heating of the substrate is a two-step process, the first involving direct heating of the substrate by the laser pulse and the second by indirect heating from recombination effects [20]. During direct heating, photons from the laser are absorbed by the carriers in the semiconductor and are promoted to an excited state until all the free states are occupied. When this happens, no more energy can be deposited. Since the electron relaxation timescale is on the order of 1-10 ps [21], the femtosecond laser beam is off by the time most of the heating occurs in the substrate. Figure 2-4 shows that the temperature of the lattice rises considerably on the picosecond timescale, far after the laser has been turned off. As the excited carriers fall back to equilibrium, the substrate is heated by phonons emitted either directly through recombination or indirectly through the thermalization of carriers due to Auger recombination. The timescale of Auger recombination is on the order of several hundred picoseconds. In the fs regime, the Auger heating is dominant and can be described by the equation

$$\rho C_p \frac{dT}{dt} = (C_e + C_h)N^3(E_g + kTH), \tag{2.2}$$

as given in [10], where H is a degeneracy factor, and C_e and C_h are the Auger coefficients for e-e-h and e-h-h processes, respectively.

A fourth model is of plasma annealing [23, 24] which explains a change in structure via a non-thermal annealing process. The rise in surface reflectivity observed in time-of-flight spectroscopy, which is usually attributed to the presence of a liquid phase, is instead interpreted as the result of an electron-hole plasma of sufficient density that $\hbar\Omega_p$ exceeds the energy of the photons used to determine the reflectivity. The electron plasma then softens the covalent bonds in the lattice allowing for the rearranging of atoms into a crystalline state. Amorphization occurs when the electron loses its mobility before the material had a chance to establish long range order.

Much work has been done to identify the mechanism for ablation. Some work indicates

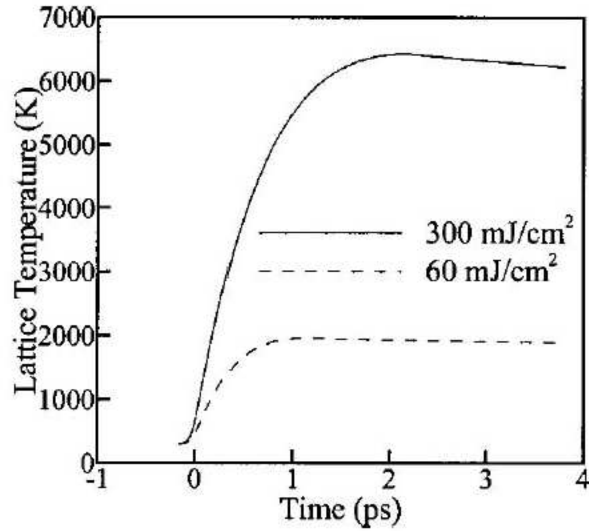

Figure 2-4: Calculated temperatures for the surface of a titanium sample at two laser fluences. Notice the delay in rise of lattice temperature [7].

a thermal effect. In some time-of-flight spectroscopy of GaAs, it has been observed that within a few hundred fs there is a rise in reflectivity in the center of the laser beam, indicating ultrafast electronic melting. After a few hundred picoseconds, the reflectivity of the entire spot increases. This timescale is significantly longer that the time needed for energy relaxation, indicating a thermal process by delayed Auger recombination. Once thermalization is complete, the material is molten and is then carried away by hydrodynamic forces [25].

Some work indicates a combination of thermal and non-thermal effects. Cavalleri et al. describes five fluence regions where at the lowest fluences, delayed auger recombination dominates. At higher fluences, melting occurs through ultrafast, non-thermal effect. Above the ablation threshold, material is removed [11]. In metals, it has been shown that the energy not used in expelling material will induce a liquid phase leading to an amorphous or polycrystalline phase during solidification [21]. There has also been a report on the oxidation of the ablated hole in addition to amorphization [9].

We believe that the ablation mechanism is a thermal effect. In our work, we are slightly

above the single-shot ablation threshold, yet we still see amorphization and surface morphology that can be attributed to a thermal process. A possible explanation of this phenomenon is that melt expulsion is occurring even in the femtosecond regime. This would indicate that electronic melting is occurring and that ablation happens by homogeneous nucleation of gas bubbles in the liquid phase.

Chapter 3

Experiments

3.1 Introduction

This chapter describes the experimental procedures used in this study. The first part discusses the laser setup and describes the characteristics of the beam. Next, we list the drilling parameters and describe the substrate. After that, there is a brief description of the methods for sample preparation for cross-sectional TEM. Finally, we give a summary of the analytical techniques used to characterize the ablated holes.

3.2 Laser Setup

The laser setup is shown in Figure 3-1. We used a Ti:Sapphire laser (Clark-MXR CPA-2000). We used a repetition rate of 50 Hz which resulted in one pulse every 20 ms. By controlling the number of milliseconds that the shutter was open, we could accurately control the number of pulses applied to the substrate. After the shutter in the laser setup, there were three mirrors that redirected the beam. Next, a quarter wave plate converted the beam from linear to circular polarization. This was to ensure the drilling of circular holes. After that, a 200 mm field lens focused the laser onto a 7.5 μm molybdenum aperture. Finally, the last two lenses, a 60 mm singlet lens and a working distance microscope objective (Mitutoyo UV80X, f =

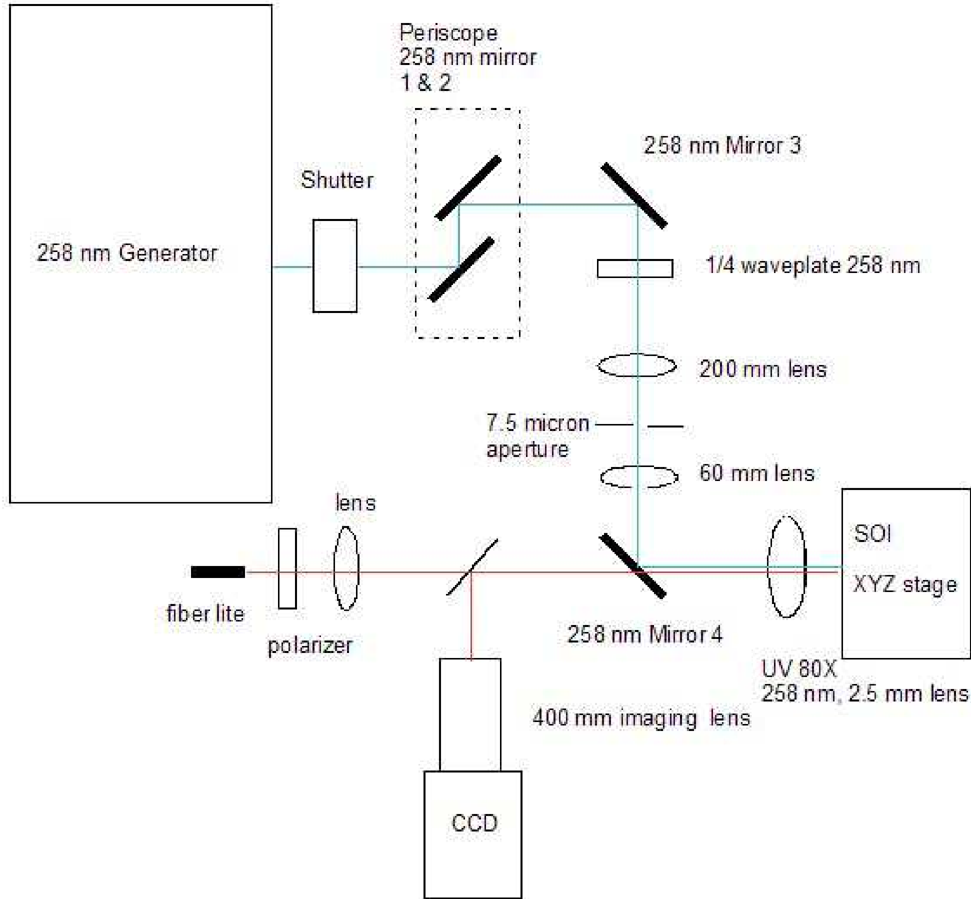

Figure 3-1: Schematic of the laser setup [4].

2.5 mm, N.A. = 0.55) acted as a microscope system which projected and shrunk the 7.5 μm aperture down to less than 500 nm.

A white light source was used to observe the drilling *in situ*. The white light beam was sent through a polarizer which optimized the light signal collected by the video camera. This light was also sent through the reverse microscope and focused on the same area as the laser beam. A video camera was mounted to the side of the white light source. This camera gave real-time feedback for observing laser damage and provided a rough estimate for the location of the laser beam.

The sample was mounted on a piezoelectric stage that was in turn mounted on a Burliegh inchworm stage. The Burliegh had XYZ freedom and had a placement accuracy of 0.5 μm.

This was used for large step movements of the substrate. The piezoelectric had two degrees of freedom (X and Y) and had accuracy of 10 nm. The piezoelectric stage was used to move the sample during drilling.

3.3 Drilling Parameters

We used a wavelength of $\lambda = 258$ nm which was frequency triple from the fundamental frequency of $\lambda = 1032$ nm. The fluence was ~ 0.1 J/cm^2. Although Φ_{TH} of Si at $\lambda = 258$ nm is not well know, through experimentation, we have deduced that we are slightly above the single-shot ablation threshold. This is based on observations of the size of many single-pulse holes in which a minimal amount of material was ablated. The laser spot diameter was about 478 nm which was calculated from the physical properties of the laser setup. This calculation is shown in Appendix A. The beam was then focused onto the substrate. For the method for focusing the laser beam, please refer to Appendix A as well.

The holes were drilled onto the front surface of a <100> silicon-on-insulator (SOI) structure with a 180 nm single-crystal Si layer on a 200 nm thick buried oxide layer. The SOI structure was purchased from SOITEC and was thinned using a hydrogen implant technique. A 3 mm by 6 mm piece was mounted onto an aluminum sample holder with silver paint. The sample holder was then attached to the vertical face of the piezoelectric stage. For some of the experiments, argon was blown over the surface at 20 psi. Otherwise, holes were drilled in open air in a high-efficiency-particle-arrestor (HEPA)-filtered laboratory maintained at 22 ± 0.5 C.

First, a 3×5 array of holes were drilled with 500 pulses in order to help locate the features. A row of 20 holes was then drilled. The first hole received one pulse and each successive hole received more and more pulses. The number of pulses varied from 1 to 100. Figure 3-2 shows the layout of the drilled holes. Finally, a 200 μm cross was drilled to facilitate the location of the drilled area.

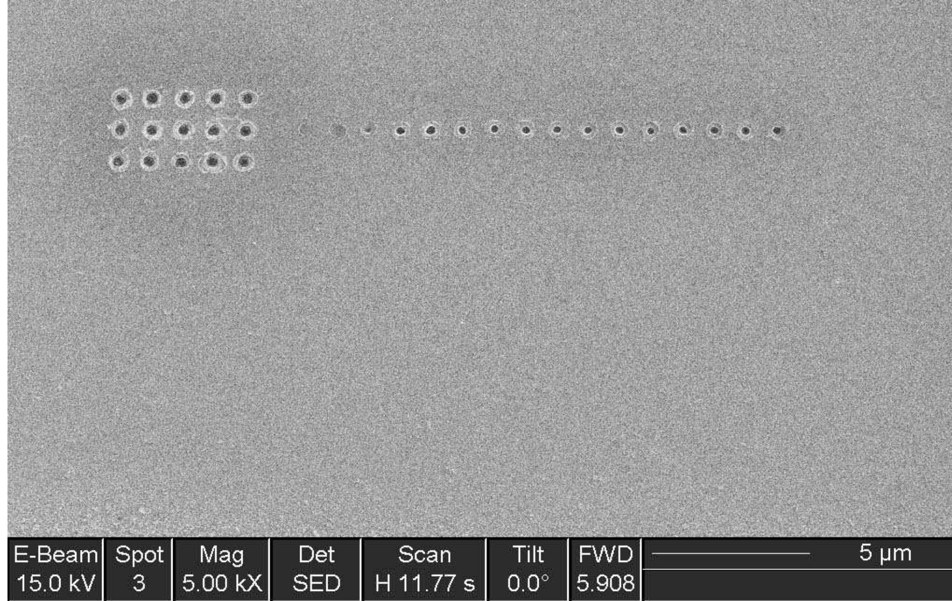

Figure 3-2: Layout of the drilled holes. There is a 3×5 alignment mark and a row of holes with increasing number of pulses.

3.4 TEM Sample Preparation

To perform a cross-sectional TEM study, we wanted to create samples with profiles of the drilled holes. Figure 3-3 shows the methodology used. The eventual goal was to mill the holes down such that the profiles of the holes were visible from both sides.For a detailed description of individual preparation steps, please consult Appendix B.

TEM sample preparation included the following steps. First, metal coatings of 10 nm Cr, 2000 nm Pt, and 500 nm Cr were deposited in succession using an electron beam evaporation technique (without a vacuum break). This was done in order to protect the holes during future processing steps. Next, sections containing the holes were cut into 200 μm wide and 3 mm long slivers using a die-saw. After that, a focused ion beam (FIB) (FEI FIB DualBeam DB235) with a gallium ion source was used to mill the sliver down to a thickness of 120-200 nm in order to make cross-sections of the holes. Figure 3-4 shows a scanning electron microscope (SEM) images of a top view of ablated holes (Figure. 3-4A) and a side view after FIB milling (Figure. 3-4B). In Figure 3-4B, it is possible to see deposited platinum plugs

inside the ablated holes.

The preparation of TEM samples by FIB is a common process and protecting the sample from the ion beam is crucial in obtaining valid results. FIB is known to damage both the side wall [26], and the surface of the samples. The side wall damage can be reduced by using a lower beam current for the final cuts. Initial cuts were made at 20 kpA and the final cuts were done at 100 pA. This limited the side wall damage to ∼40 nm on either side. The minimum thickness of our sample was 120 nm in order to assure at least 40 nm of crystalline material was sandwiched between two amorphous layers.

To protect the surface it is customary to deposit a metal layer over the sample. Ion beams are Gaussian in shape, which results in overspraying and milling outside of the intended area. Usually, depositing a micrometer of platinum *in situ* with ion-beam assisted CVD is enough to protect the sample; however, in our case, because we were interested in surface features that would be damaged by the ion beam during CVD deposition, a metal mask was deposited *ex situ*. The density of the metal determines how sharp an edge will be milled. Low density metals, such as chromium, trap stray ions not above a milling threshold which allows for good edge definitions. However, some trapped ions may penetrate the metal and amorphize the silicon underneath. High density metals, such as platinum (Pt), prevent ion penetration, forcing oversprayed ions to mill away surface atoms. This results in a much shorter lifespan for the mask as it is constantly being worn away by oversprayed ions and results in a rounded edge. Using a combination of both Pt and Cr allows protection of the surface from the ion beam and for sharp edge definition. Since Cr is used as an adhesion layer for Pt, our final mask was a sandwich structure of Cr/Pt/Cr. The final thicknesses used were found to be the best after many combinations of thicknesses were tried.

3.5 Analytical Tools

Cross-sectional TEM was done using a JEOL 2010 FEG. Unless otherwise indicated, the pictures were taken in bright field mode with the 3rd objective aperture and on the zone axis of the bulk silicon. Electron dispersive x-ray (EDX) analysis was done was done *in situ*

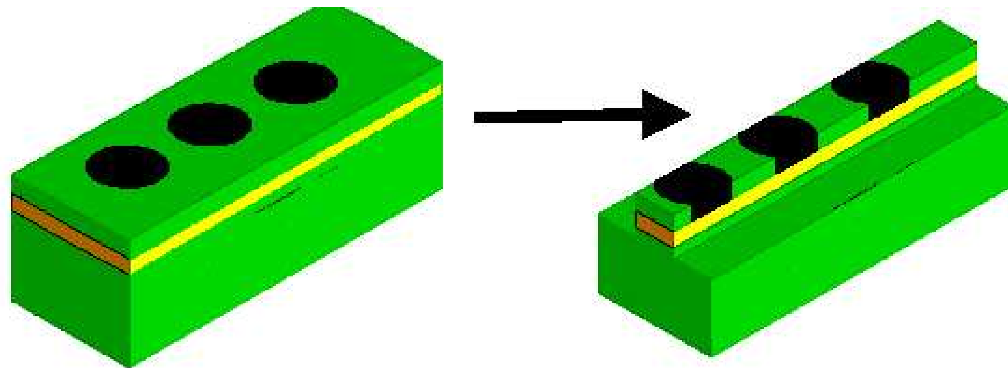

Figure 3-3: A before-and-after schematic diagram of the processing of the samples. The goal is to create profiles of the holes for TEM analysis.

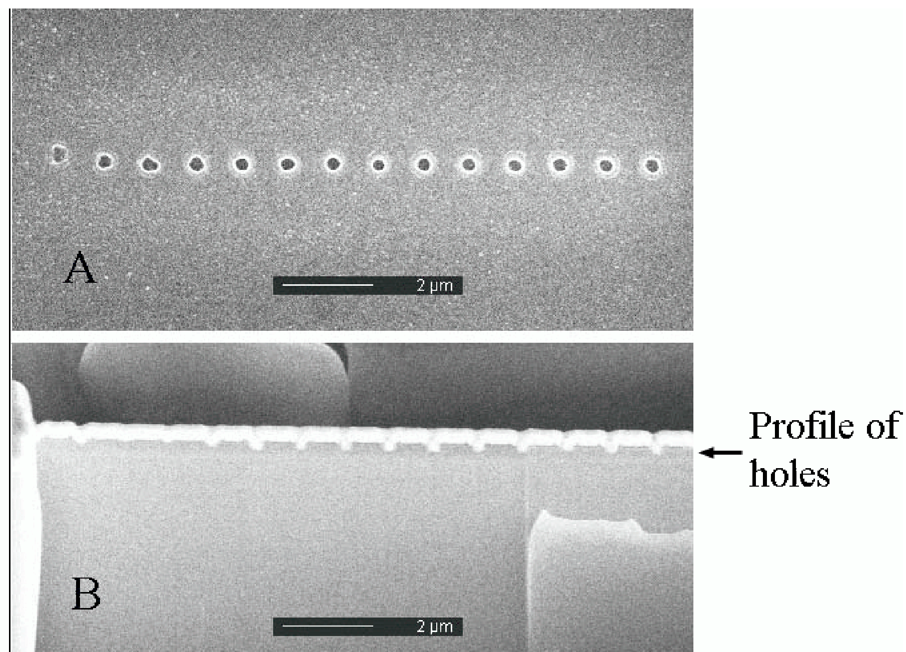

Figure 3-4: Before-and-after SEM micrograph of drilled sample. (A) SEM top view of holes (B) SEM profile after FIB milling. Note the profiles of the holes are visible.

in the TEM in scanning mode. SEM pictures were taken in the FIB.

Chapter 4

Results

4.1 Introduction

In this chapter, we will present the data that was collected from SEM, TEM, and EDX analysis. We first show SEM results for the holes. They will include analysis of redeposited Si as well as the SEM of evolution of the holes as the number of pulses increased. Next, we present a 5-pulsed sample and compare it to a 25-pulsed sample. After that, we show the elemental analysis results. Finally, we present the TEM cross-sections of holes with increasing number of pulses.

4.2 SEM results

In Figure 4-1 we see one of the 3×5 alignment hole arrays. Around the array is a sprinkling of many particles less than 100 μm in diameter. These particles were distributed evenly around the holes, even though the sample was drilled vertically. Classically, the particles should have mostly fallen to one side. Upon magnification of one of the holes, Figure 4-2, we see that the particle diameters range from 5 nm to nearly 100 nm. The number of particles can be significantly reduced by blowing argon gas at 20 psi over the silicon during drilling. As one can see in Figures 4-3 and 4-4, the sample is much cleaner and the remaining particles

are less than 20 nm.

Figures 4-5, 4-6, and 4-7 are a collage of SEM micrographs taken for range of pulses. After one pulse, there is barely any material being ablated, signifying that the laser is just barely above the ablation threshold. There are also the beginnings of a ring being formed around the ablated hole. At five pulses, we see some more ablation of the silicon and a larger ring. At ten pulses, the hole is deeper and wider. By 15 pulses, the top layer of silicon has been completely ablated. From 20 to 100 pulses, both the lip and the ablated hole increase in size. In Figure 4-8, one can see the diameters increase rapidly in the beginning and then level off at high number of pulse values. Outside of this lip, there is no modification to the silicon substrate.

4.3 TEM Results

Figure 4-9 is a TEM micrograph of an undrilled area. Many different layers are clearly visible. There are three metal deposition layers (A,B,C) as well as the SOI structure underneath (E,F,G). Native oxide layers are generally on the order of 1-3 nm thick which is comparable to layer (D).

Figure 4-10 shows a typical cross-sectional TEM micrograph, in which metal and SOI layers can be observed, along with a layer of Si (H) in the laser-affected zone that has a different contrast from the single crystal silicon (c-Si). Layer (H) is considerably thicker than layer (D) - 60 nm thick at its thickest point and 13 nm at the center of the hole. The width of layer (H) is 652 nm, and the depth is 129 nm. Near the rim of the hole, we can see that layer (H) protrudes above the surface of the c-Si by 25 nm. These protrusions are the lips seen in the SEM micrographs.

In Figure 4-10, layer (H) does not display any lattice fringes, unlike the c-Si layer. Also the transmission electron diffraction pattern is characteristic of an amorphous layer. The Cr adhesion layer is deposited uniformly over layer (H); thus layer (H) must have formed before metal deposition. This would eliminate FIB-milling as a source for amorphization since FIB milling occurred after metal deposition.

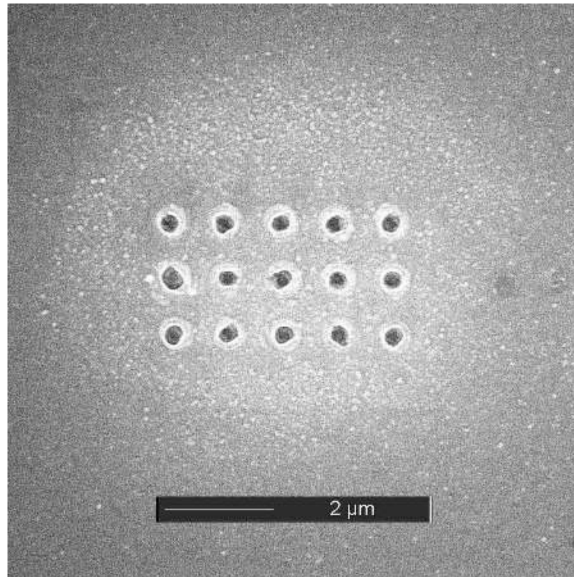

Figure 4-1: Particles splattered $\sim 2\mu$m diameter around the 3×5 alignment holes.

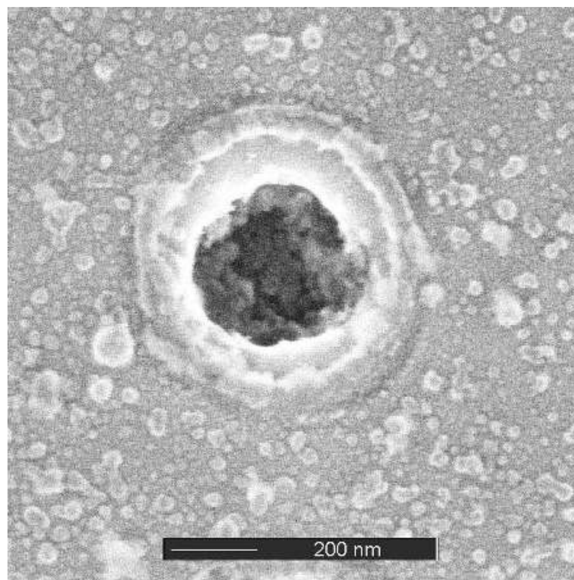

Figure 4-2: High magnification of one of the alignment holes. Particles < 100 nm in diameter are scattered around a 500-pulsed hole.

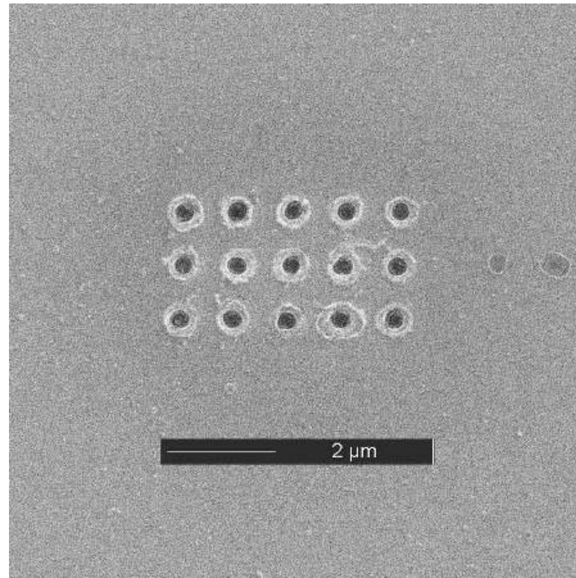

Figure 4-3: Fewer particles are found around the alignment holes when 20 psi of argon is blown over the surface during drilling.

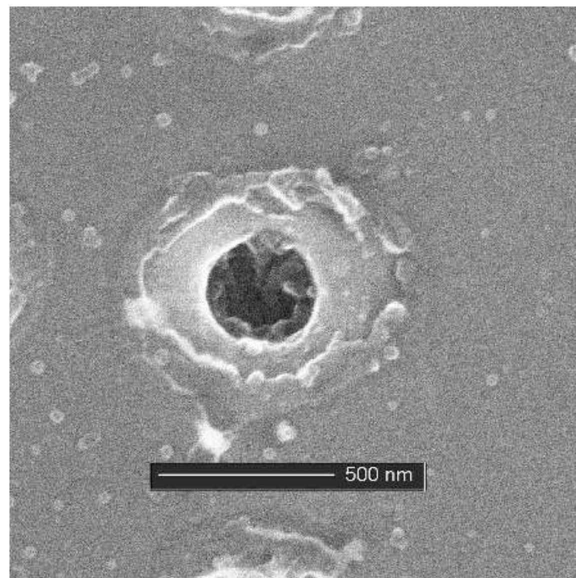

Figure 4-4: High magnification of a 500-pulsed hole with 20 psi of argon blown during drilling. Particles are now < 20 nm in diameter.

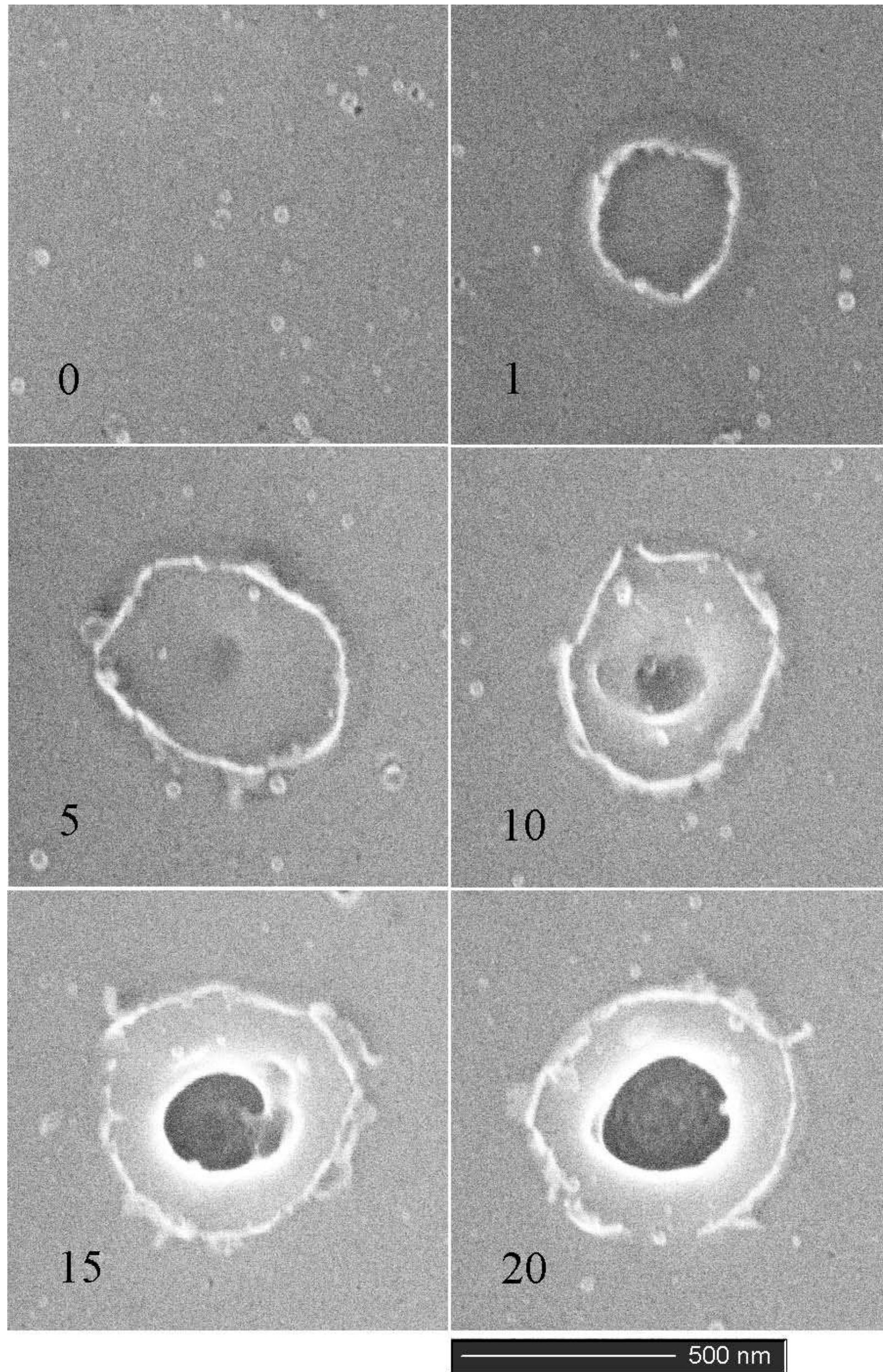

Figure 4-5: SEM micrograph of drilled holes with various numbers of pulses.

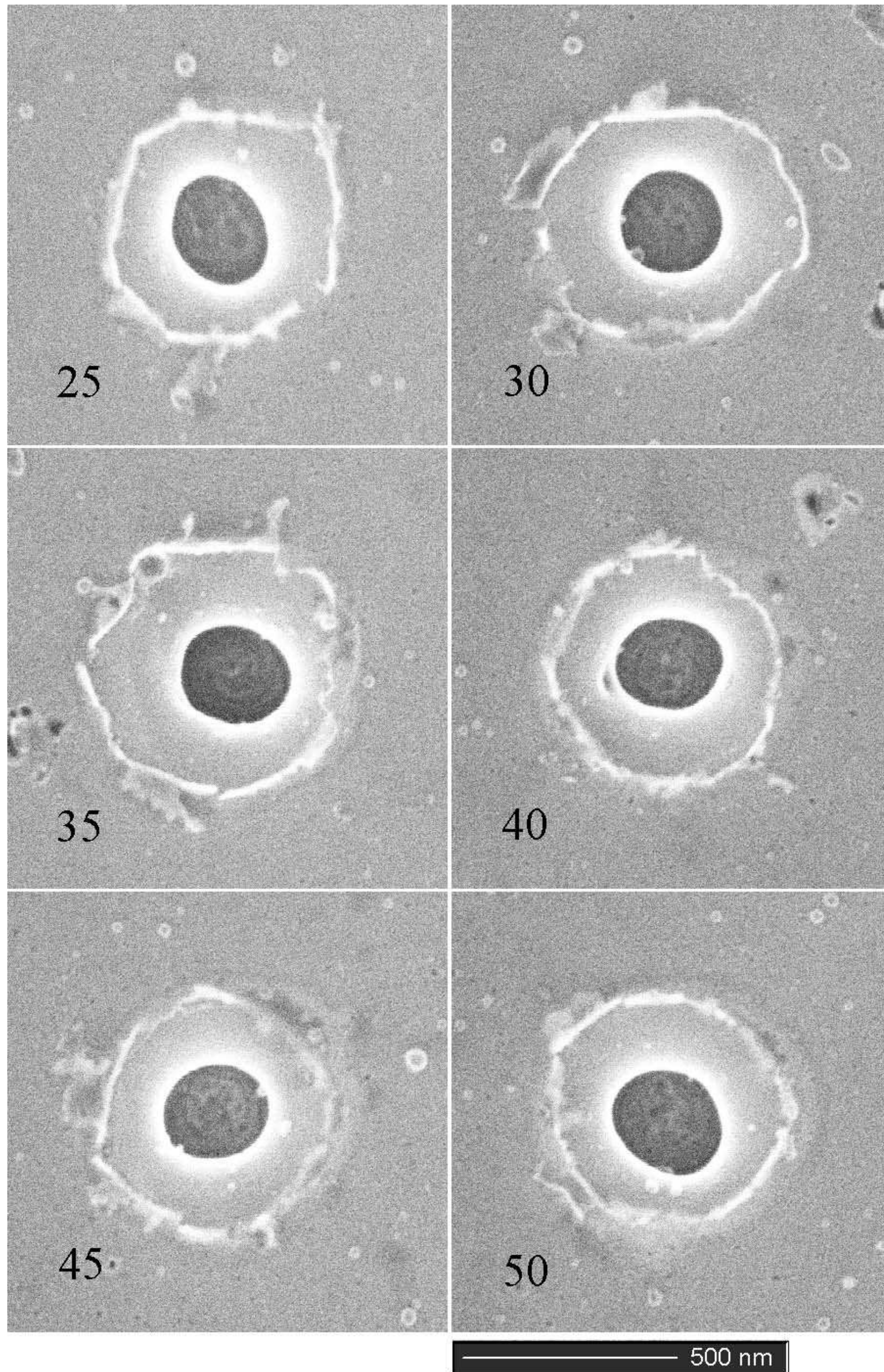

Figure 4-6: SEM micrograph of drilled holes with various numbers of pulses, cont.

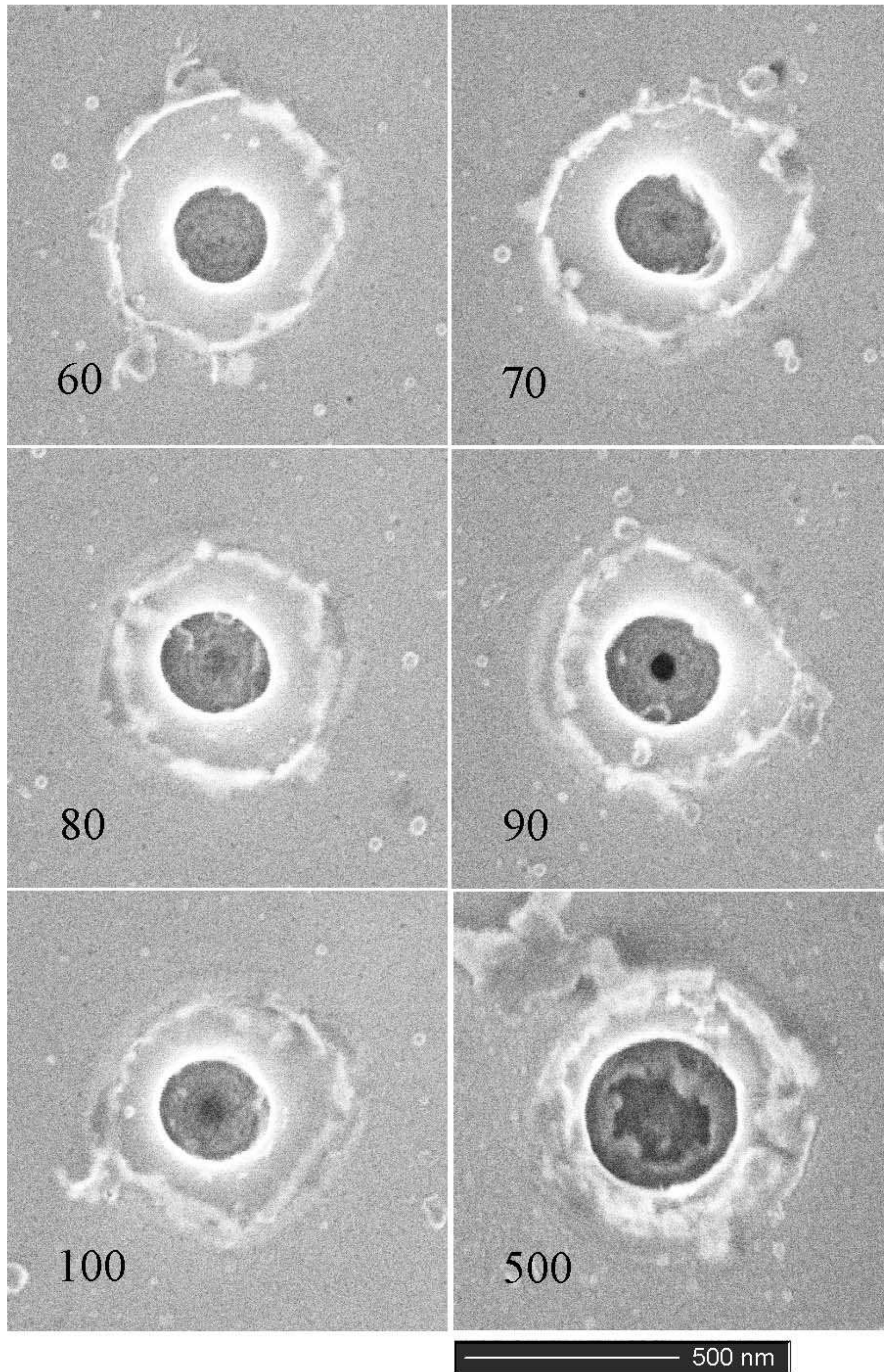

Figure 4-7: SEM micrograph of drilled holes with various numbers of pulses, cont.

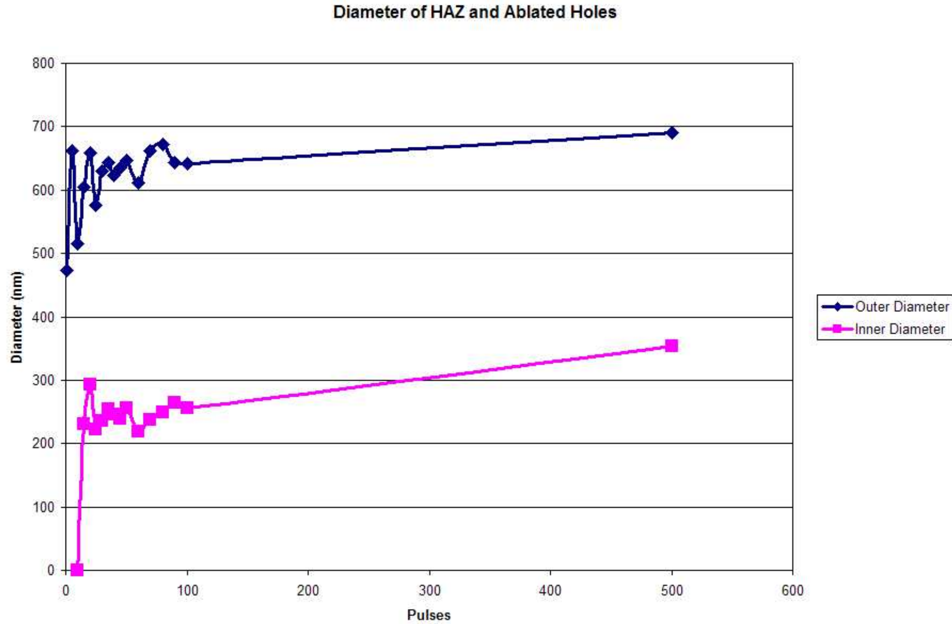

Figure 4-8: Measurements of the diameter of the heat affected zone and the ablated hole vs. number of pulses as measured from the SEM micrographs.

The silicon dioxide, layer (F), is also amorphous. An elemental study was performed to characterize the laser modified layer (H) to determine if it could be amorphous SiO_2. Figure 4-11 is the EDX spectrum of layer (H). We see trace amounts of Pt and Cr which are expected because they were used as masks. We also see trace amounts of Ga which are also expected because the FIB used a Ga ion beam. The largest peak is that of silicon. For comparison, Figure 4-12 is the EDX spectrum of layer (F). Here, we also see trace peaks for Pt, Cr, and Ga, but we also see a substantial oxygen peak about half the size of the silicon peak. In comparing these two spectrums, we can conclude that the modified region is amorphous silicon that results from laser-matter interactions. Even though the sample was drilled in air, oxides did not form. This confirms the observation that there is no difference in material property changes for drilling in vacuum or in ambient air [30].

After 25 pulses, complete ablation of the top layer of silicon can be seen in Fig. 4-13. Both Fig. 4-13A and Fig. 4-13B are taken of the same hole. Figure 4-13A is taken on the zone axis and Fig. 4-13B is taken on the <110> plane. The main difference is that on

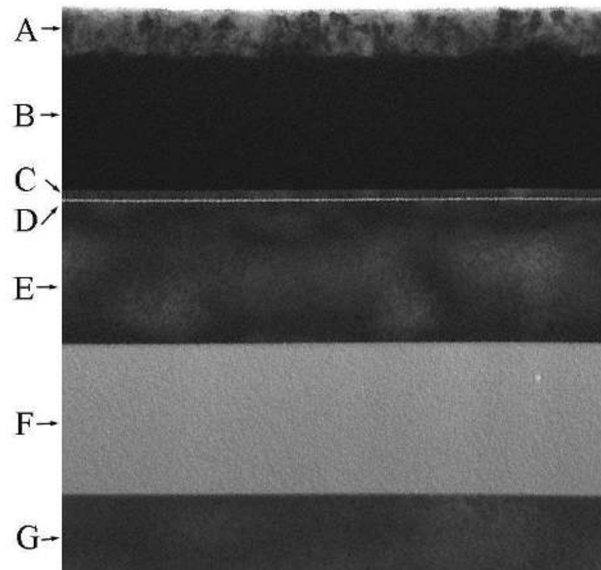

Figure 4-9: A TEM micrograph of a region unmodified by the laser beam. (A) Top layer of Cr, (B) Pt, (C) Cr adhesion layer, (D) silicon native oxide, (E) top layer Si, (F), buried oxide, and (G) bulk silicon.

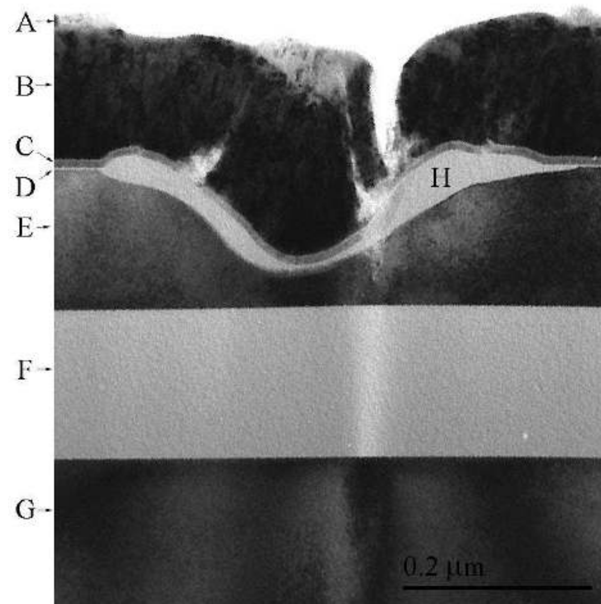

Figure 4-10: Cross-section TEM Micrograph of a five-pulsed hole. (A) Top layer of Cr, (B) Pt, (C) Cr adhesion layer, (D) silicon native oxide, (E) top layer Si, (F) buried oxide, (G) bulk silicon, and (H) laser modified layer.

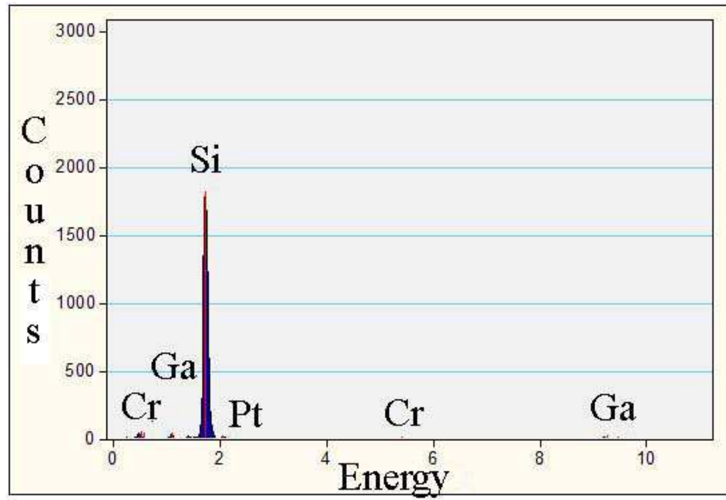

Figure 4-11: EDX spectrum of the modified region (H) in Fig. 4-10. Note the large Si peak

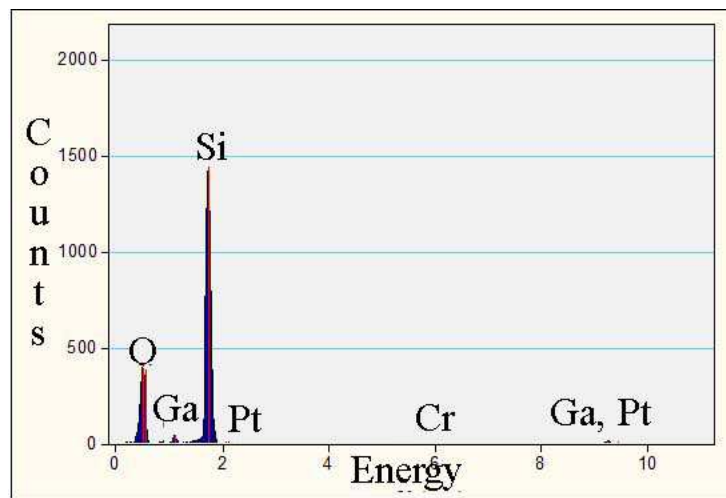

Figure 4-12: EDX of the buried oxide, layer (F) in Fig. 4-10. There is a substantial oxide peak.

the zone axis, amorphous material has a light contrast and crystalline material has a dark contrast. On the <110> plane, that is reversed. Some features are more easily observed in one imaging mode than the other.

Twenty-five nm high protrusions are visible above the surface of the silicon, corresponding to the lips in the SEM micrographs. The width of the hole at the surface is 625 nm. There are two lighter regions around the platinum plug in the hole. Those regions are empty space that was formed during evaporative deposition. Metal deposits at the bottom of the hole at the same rate that it deposits at the top. Eventually a ledge forms near the surface, preventing continual deposition in the hole. An interesting feature is that the top silicon layer seems to have been undercut. The diameter of the hole half-way down the top layer of silicon is 277 nm and the diameter at the Si/SiO_2 interface is about 353 nm. There is also amorphous material in the bulk silicon below the buried oxide. Inside the oxide is a bubble shaped like a lens.

There are several features that can be discerned better from the <110> plane (Fig. 4-13B). There are 20-30 nm of modified material around the top and sides of the hole. The modified layers do not all correspond to the amorphous regions seen in Fig 4-13A. A possible explanation is that the hole is curved, and we may be observing amorphous material through crystalline material. We also see substantial modification of the bulk silicon underneath the oxide. This region is 315 nm in diameter and has a depth of 53 nm. Further observations of the bulk modification and the bubble can be made from their evolution with increasing number of pulses.

4.4 Evolution with Increasing Number of Pulses

Figures 4-14, 4-15, and 4-16 are a collage of TEM micrographs taken with increasing numbers of pulses. In this set of experiments, the metal layer delaminated from the substrate so there is a white layer corresponding to a lack of material. Because the sample was machined using an FIB, some milled debris deposited in this empty space, resulting in a fuzzy area around the lips of the holes. However, we can still use the micrographs to investigate effects below

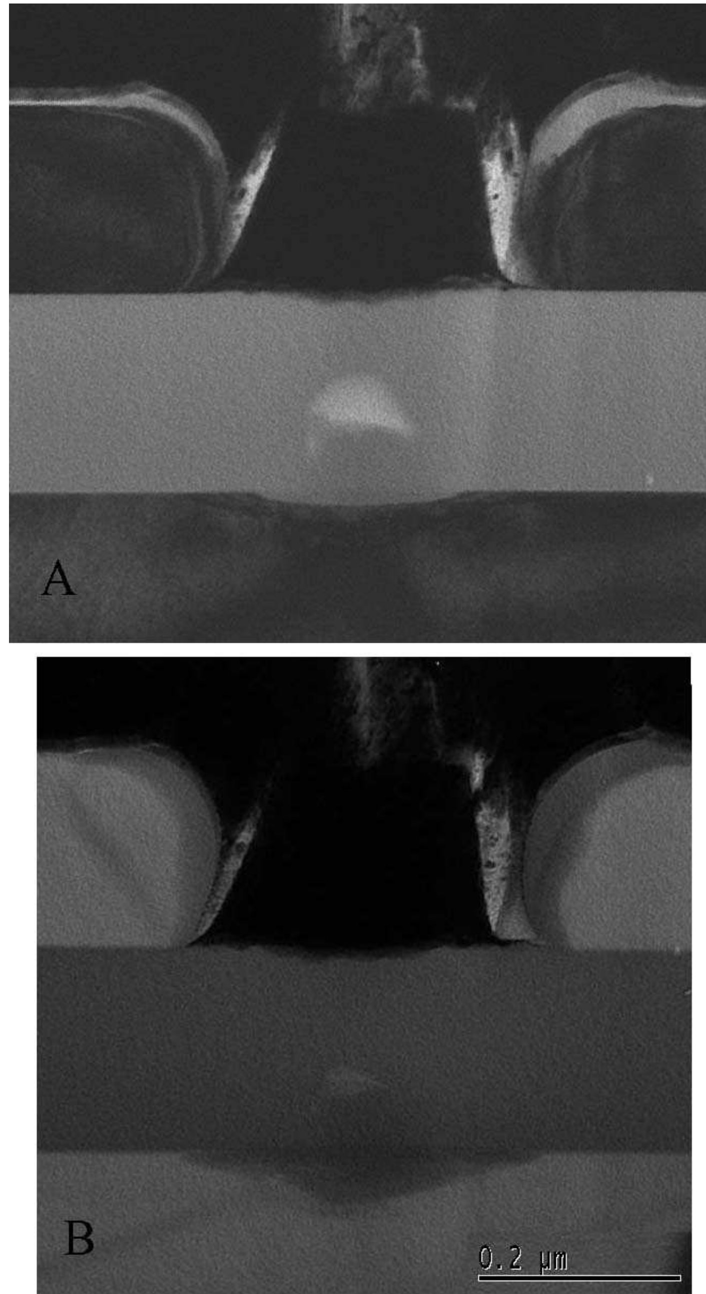

Figure 4-13: Cross-sectional TEM of a 25-pulsed hole where the top surface is completely ablated. (A) is taken on the zone axis. (B) is taken on the <110> plane.

the surface.

The holes became larger as the number of pulses was increased. Figure 4-17 shows the evolution of the diameters of the hole at the top surface, at a point half-way down the hole, and at the interface between bulk Si/SiO_2. By 10 pulses, the top layer of silicon is ablated away. By 15 pulses, we begin to see some undercutting of the top layer. All of the features increase with increasing numbers of pulses. The amorphous material on the side of the holes is present in all the holes.

After the top layer of silicon is ablated away, there is also modification of the silicon under the oxide. Since the oxide has a much higher ablation threshold than the silicon, the laser beam can pass through the oxide. After 10 pulses, we begin to see evidence of modified material. As the number of pulses increase, the size of the modified region grows larger as seen in Figure 4-18. The region has a smooth, curved edge until 30 pulses when the edge becomes uneven. After 50 and 60 pulses, crystallization to a polycrystalline material in the Si below the SiO_2 layer is apparent. At 60 pulses, the crystalline protrudes above the original bulk Si/SiO_2 interface.

Figure 4-19 shows the recrystallized area in the 60-pulsed sample at a 500 kX magnification. The micrograph was taken with the 2nd objective aperture. There is 21 nm of material protruding above the original bulk Si/SiO_2 interface. Several areas were magnified further to observe the crystal structure. In Figure 4-20, we can see that the tip of the darker material is indeed crystalline, meaning that the silicon grew into the oxide layer. This means that there must have been a gap in the oxide for that to happen. Figure 4-21 shows that the crystallized material is not a single crystal but polycrystalline. This seems to indicate that depending on the cooling rates, the molten bulk silicon may solidify as either amorphous silicon or polycrystalline silicon. [22].

There is the formation of a bubble in the oxide layer. As the number of pulses increase, the bubble grows larger and rises to the top surface of the oxide. By 40 pulses, the bubble becomes fairly circular and continues its ascent towards the top. By 60 pulses, the bubble breaks through the surface. At 90 pulses, there are several bubbles, a big, main one, and two

smaller ones. At 100 pulses, we can see several new bubbles nucleating at the bulk Si/SiO_2 interface.

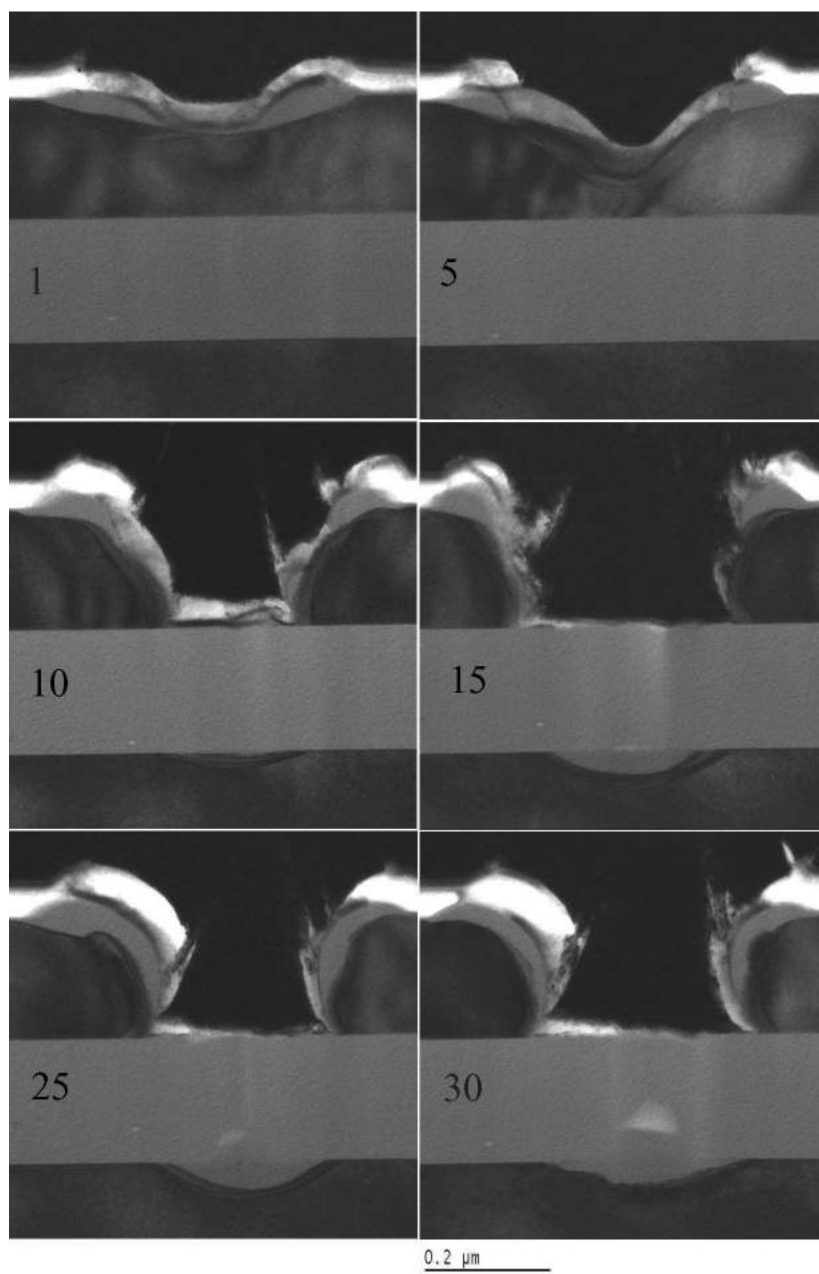

Figure 4-14: TEM cross-sectional micrographs of holes ablated for various numbers of pulses.

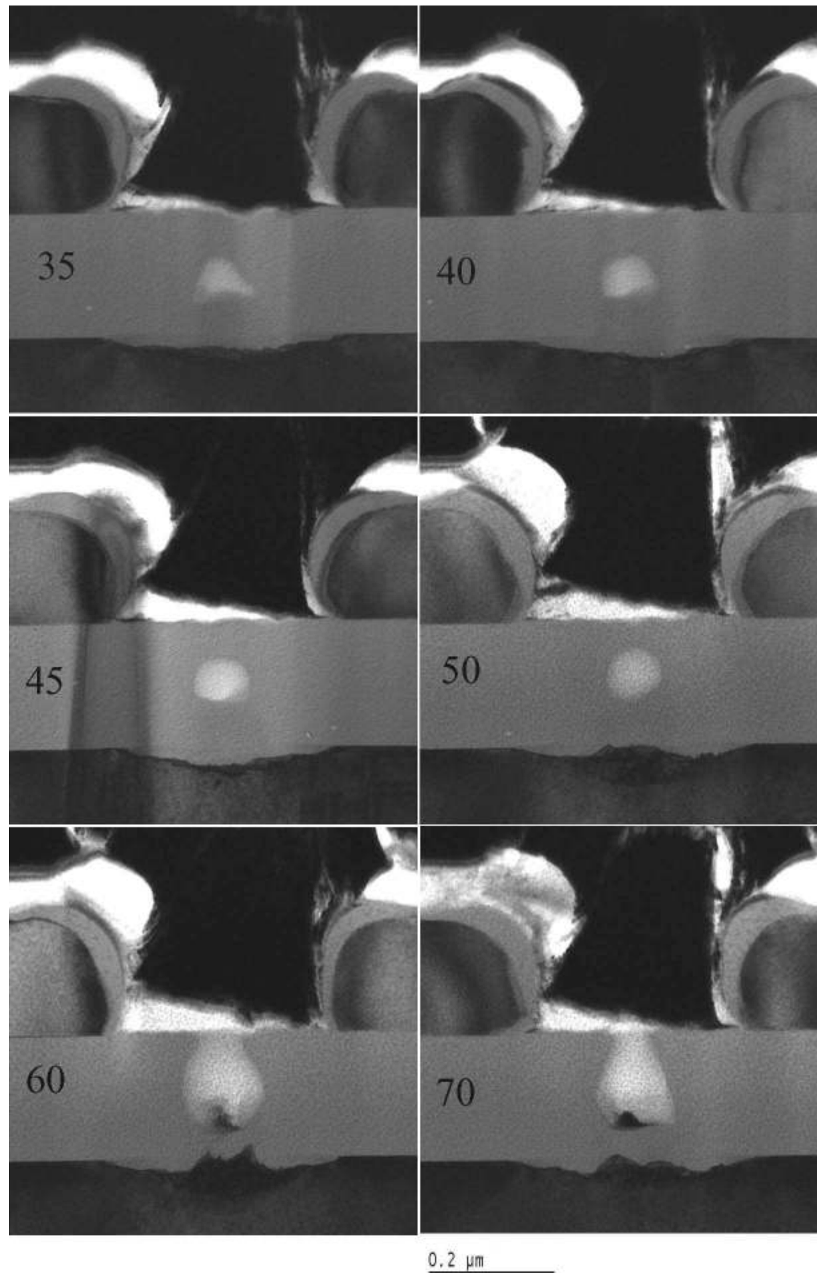

Figure 4-15: TEM cross-sectional micrographs of holes ablated for various number of pulses, cont.

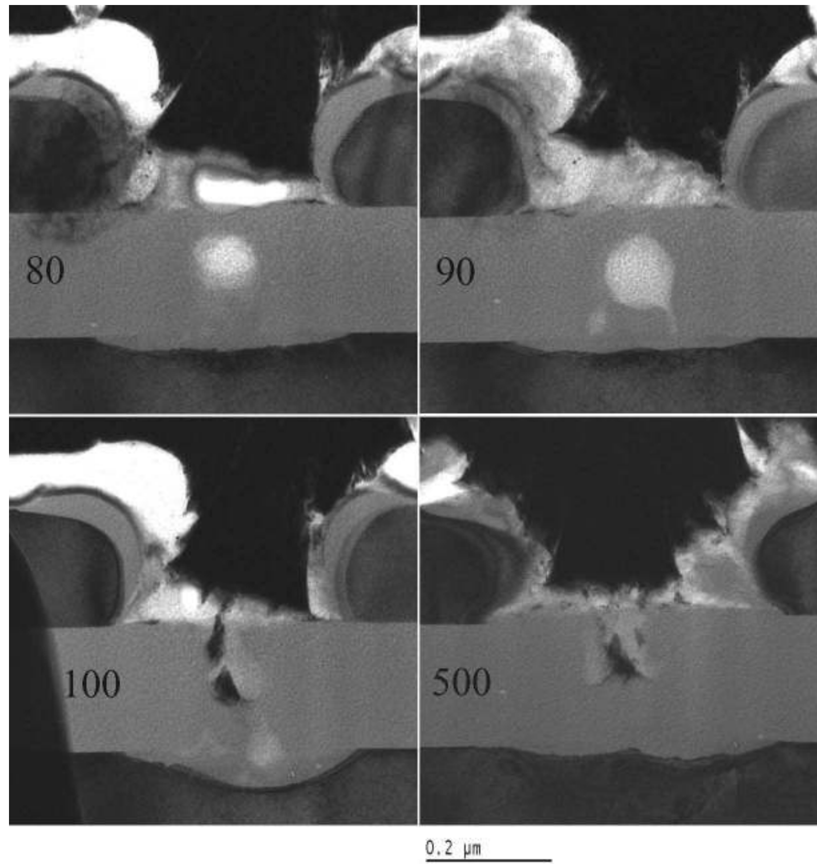

Figure 4-16: TEM cross-sectional micrographs of holes ablated for various number of pulses, cont.

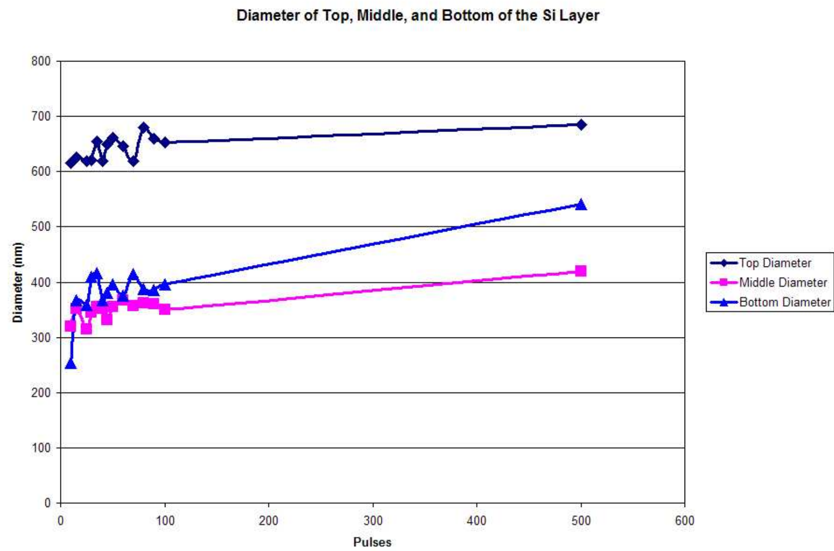

Figure 4-17: Diameters of holes from the TEM micrographs. They are measured at the top, middle and bottom of the top layer Si (layer (E) of Fig. 4-10). Note the diameter of near the interface of the bulk Si/SiO_2 is larger than the diameter of the middle.

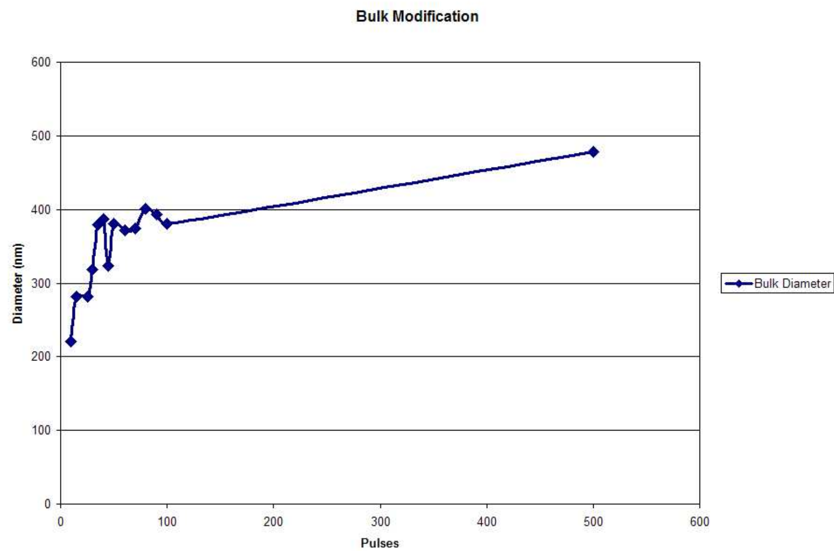

Figure 4-18: Diameter of the modified region in the bulk silicon.

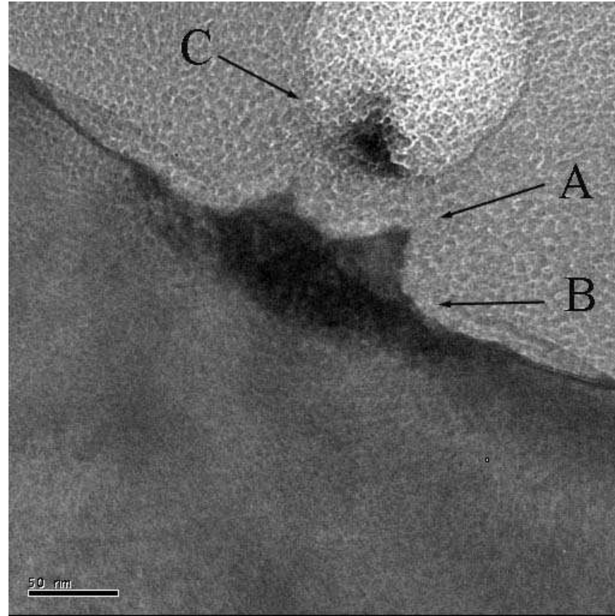

Figure 4-19: TEM micrograph of the modified area in the bulk silicon under the oxide after 60 pulses. (A) is recrystallized into the oxide (see Fig. 4-20) (B) is a polycrystalline region (see Fig. 4-21) (C) is crystalline material in the bubble (see Fig. 4-22).

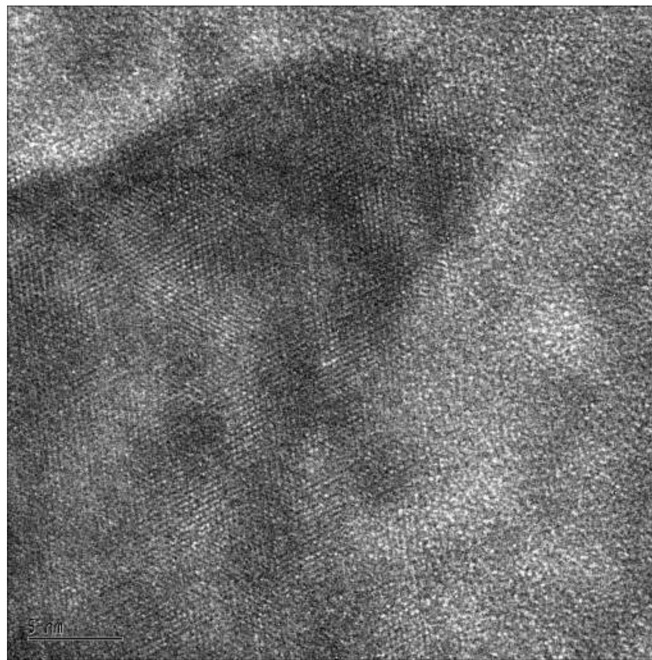

Figure 4-20: Region (A) in Fig. 4-19. Tip of the modified region that protrudes into the oxide. We can see lattice fringes indicating crystalline features in the oxide.

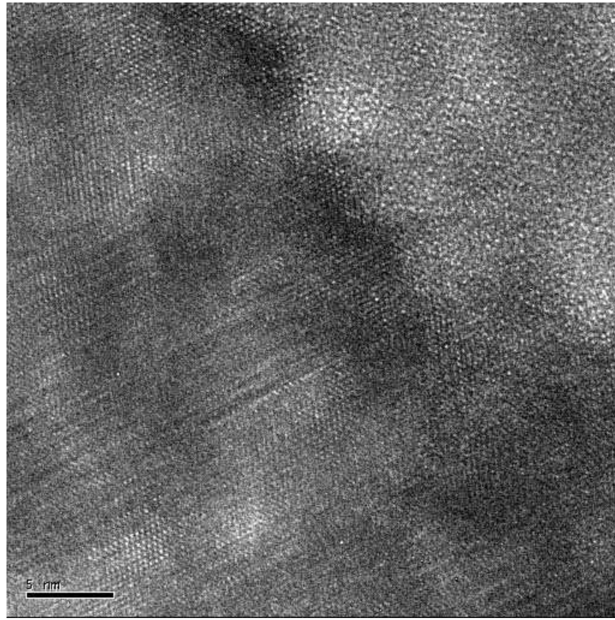

Figure 4-21: Region (B) in Fig. 4-19. Lattice fringes for polycrystalline material under the oxide.

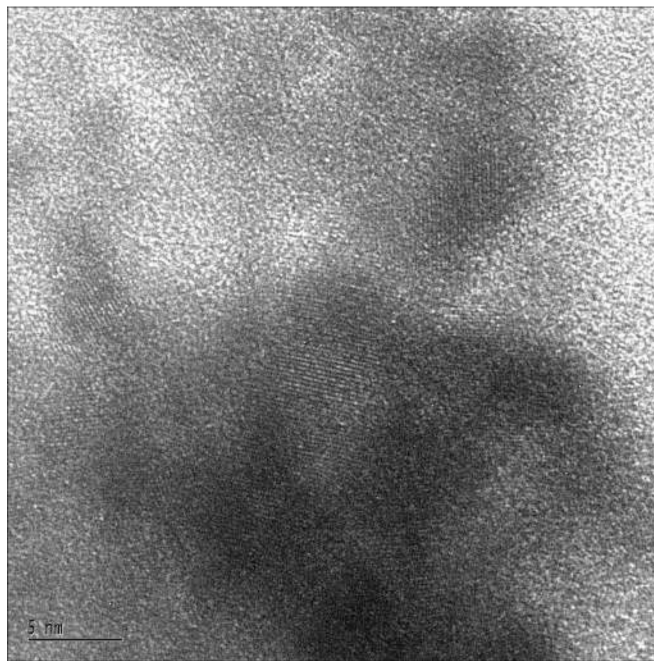

Figure 4-22: Region (C) in Fig. 4-19. Lattice fringes indicating crystalline material in the bubble.

Chapter 5

Discussion

5.1 Introduction

In this chapter, we will analyze the results described in the previous chapter. The origin of amorphization and its implication of melting will be discussed. We will introduce a thermal model to describe the mechanism. Length scales of the ablation effects will also be discussed. Finally, we will discuss some of the indications of melting from some of the secondary effects of laser ablation, such as the undercutting of the device layer of silicon and the amorphization of the bulk silicon below the buried oxide.

5.2 Amorphization

The presence of amorphous silicon (a-Si) implies the presence of liquid silicon (l-Si). Amorphous-Si is formed by the undercooling of l-Si when the cooling rate of the liquid is too fast for the nucleation of crystalline silicon (c-Si) or the propagation of an existing liquid-crystal interface. Two theories account for amorphization of silicon, that of plasma annealing and that of thermal melting. In plasma annealing, silicon is amorphized due to the breaking of bonds by an excess of electrons and not by the rise in temperature. However, the formation of the lip around the holes gives evidence for a thermal effect. In Figure 4-10, there is a

protrusion of the amorphous material above the surface of the silicon near the edge of the hole. During ablation, the pressure of vapor expanding from the surface can be several to many hundred GPa's [2, 27]. Material is pushed above the surface via melt expulsion, similar to the mechanism in the nanosecond regime. When the liquid solidifies to the amorphous state, protrusions are left behind. Plasma annealing does not account for the formation of the lips.

Amorphous silicon forms if there is sufficient undercooling of the melt that the solidification velocity is too fast for crystallization. The undercooled temperature must be 200-300 K below the a-Si equilibrium melting point. The melting point of a-Si is estimated to be 1420 K which is about 230 K below that for crystalline Si [28]. The cooling rates during resolidification can reach 10^{13} C/s [29]. The estimated critical velocity for amorphization has been calculated to be 18 m/s. Crystal growth has been observed to occur up to a rate of 15 m/s [31]. Our repetition rate is 50Hz, or one pulse every 20 ms. In our experiments, the thickest amorphous layers are 60 nm, which would take 4 ps to resolidify. Thus in our experiments, the silicon substrates completely solidifies before the application of subsequent pulse.

Some people have identified a modification threshold below which there is no observable change in surface morphology [9]. This threshold is slightly below the ablation threshold. Thus, laser-matter interaction for single pulsed lasers have been split into three regimes: (1) above the ablation threshold there is ejection of material with no amorphization inside the hole, (2) between the modification and ablation threshold where there is modification of the material, and (3) below the modification threshold where there are no observable effects. As far as we know, no one has been able to directly observe the modified silicon.

5.3 Calculations

To further understand the melting phenomenon, the incident energy was compared to the energy it would take to thermally vaporize a given volume of silicon. First, the change in enthalpy, ΔH, necessary to bring silicon from room temperature to the gas phase was calculated by summing all of the individual heating steps

$$\Delta H_s = \int_{RT}^{T_m} Cp_s dT \tag{5.1}$$

where $T_m = 1683K$ [33], $RT = 293K$, and Cp_s is the heat capacity of solid Si.

$$\Delta H_{s\to l} = 1800 J/g [32] \tag{5.2}$$

$$\Delta H_l = \int_{T_m}^{T_v} Cp_l dT \tag{5.3}$$

where $T_v = 2628K$ [33] and Cp_l is the head capacity of liquid Si.

$$\Delta H_{l\to v} = 10,606 J/g [32]. \tag{5.4}$$

The heat capacities were were taken to be

$$Cp_s = 2.33 \frac{T - 157}{T - 99} J/gK [34] \tag{5.5}$$

and

$$Cr_l = 3R + 4.8 \times 10^{-4} T + 4.157 \times 10^5 T^2 - 1.002 \times 10^{-7} T^2 J/gK [35]. \tag{5.6}$$

At equilibrium melting, $\Delta G = 0$. This means

$$\Delta S = \frac{\Delta H_m}{T_m}. \tag{5.7}$$

Thus,

$$\Delta G_m = \int_{RT}^{T_m} Cp_s dT + \Delta H_m - RT \frac{\Delta H_m}{T_m} \tag{5.8}$$

where ΔH_m is the sum of equations 5.1 and 5.2 and

$$\Delta G_v = \Delta G_m + \int_{T_m}^{T_v} Cp_l dT + \Delta H_v - RT \frac{\Delta H_v}{T_v} \tag{5.9}$$

where ΔH_v is the sum of equations 5.3 and 5.4. Evaluating equations 5.8 and 5.9, we obtain

$$\Delta G_m = 10.3kJ/cm^3 \tag{5.10}$$

$$\Delta G_v = 34.2kJ/cm^3. \tag{5.11}$$

The amount of energy deposited was calculated assuming a Gaussian distribution of the laser beam energy,

$$f(x) = I_0(2\pi r)exp\left[-\frac{r^2}{\sigma^2}\right]. \tag{5.12}$$

The values for I_0 and σ are derived in Appendix A. We can now integrate over an area to find the total amount of energy deposited

$$E_{tot} = \int_0^r f(r)drl \tag{5.13}$$

The intensity of the laser can fluctuate by 50%. If we assume an area with a radius of 25 nm, by using equation 5.13 we find that 1.96 $\pm$ 0.9 pJ is deposited by the laser beam.

By inspection of the 1 pulsed hole in Figure 4-14, it is estimated that 20 nm of material is ablated. The amount of energy it would have taken to remove a volume of material 20 nm deep with a radius of 25 nm can be found by multiplying ΔG_v by the volume ablated. This is found to be 1.34 pJ. With the remaining energy deposited by the laser beam, we can melt 30 $\pm$ 43 nm of silicon.

Since the ablation mechanism is via melt expulsion, not all of the ablated volume is removed in the vapor phase; some is expulsed in the liquid phase. In this case, it would take less energy to ablate the same volume of material. This calculation is an upper bound of the energy necessary to ablate silicon.

The lower bound of the calculation is to assume that the laser energy only melts the silicon with no vaporization occurring. In this case, 96.7 $\pm$ 44.3 nm of silicon would melt. Our experimental observations fall between these two calculated boundaries, indicating some combination of melting, vaporization, and melt expulsion via vapor pressure as a mechanism

for ablation.

5.4 Length Scales

There are three length scales of interest. The first is the splatter zone of particles around the hole. The second is the size of the heat affected zone. The third is the size of the ablated hole.

In Figure 4-1, there are ∼100 nm particles distributed evenly around the 3 x 5 alignment mark. The splatter zone is on the order of the 2 μm. That the particles are evenly distributed was unexpected because the sample was mounted vertically. A possible explanation is that if material was expelled as particle they may be deflected back to the surface by dust particles in the air. If ablation occurs via a vaporized plume, the plume may expand and rapidly cool at the plume/surface interface. This could cause rapid nucleation and growth of silicon particles. By blowing a steady stream of argon at 20 psi, many of the surface particles can be removed (Fig. 4-3, 4-4). It is, however, impossible to tell whether the plume consists of Si vapor or Si particles, only that they were prevented from redepositing near the hole. The TEM micrographs were taken of samples without a steady stream of argon gas, but the surface particles are not visible. This is because they are obscured by the deposited metal. Since the particles are smaller than the thickness of the sample after FIB milling, the particles are effectively covered by the metal mask.

The heat affected zone for femtosecond ablation has been directly observed in this study. Amorphization of the surface and the sides of the hole occurs to a depth of 30 nm thick which is significantly less than the HAZ for ns ablation. The diameter of the extent of the HAZ increases as the number of pulses increase. Figure 4-8 shows the evolution of the diameter of the heat affected zone of the hole in Figures 4-5, 4-6, and 4-7. At 500 pulses, the hole diameter is only 689 nm, on the order of the spot size, which is 478 nm. This analysis indicates that even in the fs regime, there is a heat affected zone.

The diameter of the ablated hole increases with increasing number of pulses. After 15 pulses, the surface is completely ablated, and the hole is 230 nm in diameter. This increases

with increasing number of pulses to 354 nm after 500 pulses. As one can see from Figure 4-17, the rate of increase in hole size decreases with the number of pulses. This is because only the tip of the laser beam is above the ablation threshold. Material outside the region where the ablation threshold is reached will not be removed.

5.5 Secondary Effects

The surface features, such as the amorphized region and the protrusions, indicate a thermal effect. The secondary effects, effects that occurred below the surface, also give such indications. In Figure 4-14, from 15 pulses onwards, there are several secondary effects that are worth discussing, namely the undercutting of the top layer of silicon, the melting of the bulk silicon, and the evolution of the bubble in the oxide.

Bulk melting is observed after 15 pulses in Figure 4-14. For bulk melting to occur, the laser beam must be above the modification threshold after transmission through the oxide. Since the ablation threshold for oxide is higher than the ablation threshold for silicon, the oxide is not visibly damaged. The laser beam is conical in shape and the focal depth (FD) is ~ 1 μm. The calculation of FD is done in Appendix A. Within that 1 μm, the laser beam is above threshold. Since the top layer of Si is only 0.2 μm, and the SiO_2 is also 0.2 μm, it is possible that the FD of the laser beam extends into the bulk silicon. Figure 5-1 demonstrates the melting effect. After melting, the bulk silicon may cool rapidly to the amorphous stage or recrystallize. In Figure 4-21, we see polycrystalline material. This indicates that in this case the single crystal bulk Si must have melted and recrystallize as polycrystalline material.

There are several indications that the feature is a void which may be filled with gas. First, whenever the bubble rises to the top and breaks through the surface, a bit of dark matter is found at the bottom of the bubble. This dark matter is polycrystalline, shown in Figure 4-22. The material must be Cr adhesion layer deposited into the hole during metal deposition. For Cr to deposit, the bubble therefore must be empty or filled with gas.

The bubble inside the oxide nucleates at the bulk Si/SiO_2 interface after 15 pulses and rises towards the surface. If the laser melts the bulk silicon, stresses may form at the bulk

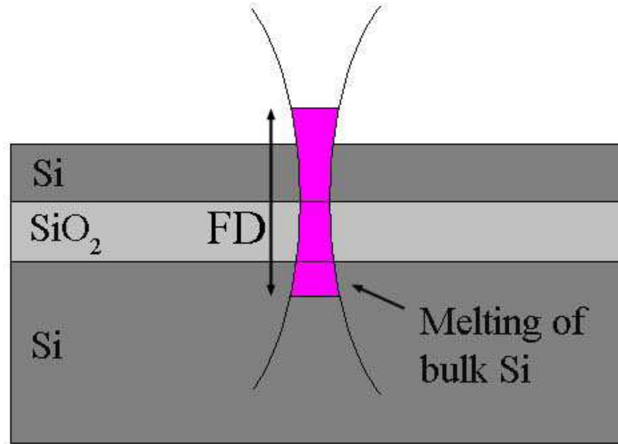

Figure 5-1: The FD of the laser can spread into the bulk silicon. This may cause the melting of the bulk material.

Si/SiO_2 and cause cracking. The laser can soften the oxide by electronic heating, and the glass may flow so that the volume of the crack coalesces. The bubbles eventually become round, indicating the oxide softens significantly. The oxide may be softened due to a rise in temperature that makes the oxide flow more easily. The bubbles rise and eventually break through the top surface. This process repeats itself, as more bubbles can be seen forming even after one bubble has broken the surface in Figure 4-15 after 100 pulses. The composition of the bubble is a mystery. It was suggested that it may be hydrogen as the device layer silicon is silicon is cleaved through a hydrogen implantation process. Another possibility is that the bubble is filled with oxygen. The oxide is thermally grown, resulting in the super-saturation of the silicon oxide with O_2 gas. The gas may become trapped while diffusing through the oxide layer to react with the silicon. The O_2 can be released when the temperature is raised during pulsed laser irradiation.

That the bubble's nucleating at the surface of the bulk Si/SiO_2 interface indicate the bulk silicon can solidify above the oxide layer. Figure 4-19 clearly shows that material resolidified above the interface, and Figure 4-20 shows that the solidified material is crystalline. The oxide layer is thermally grown which is known to be very dense. Only if there is an empty space at the interface can the bulk silicon recrystallize into it.

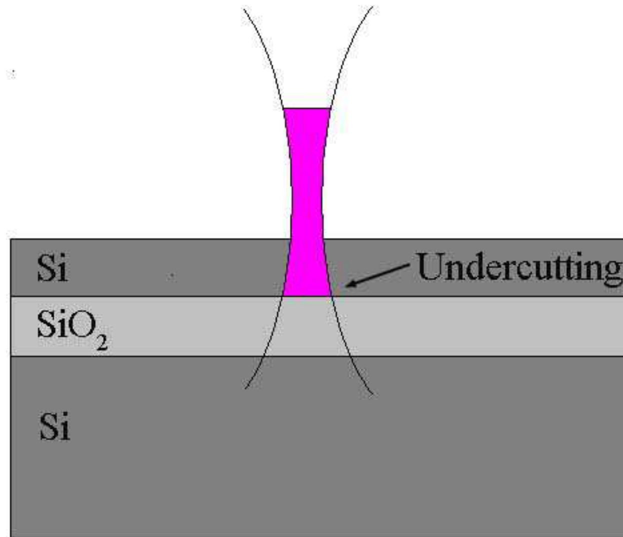

Figure 5-2: If the laser is focused too high, undercutting may occur due to the spread of the laser beam.

There is also undercutting of the top layer of silicon. One possible mechanism is that the spatial intensity distribution of the laser beam may cause the undercutting. The distribution is known to affect the geometry of a drilled feature [36] (Figure 5-2). This mechanism is rather unlikely as we used the same phenomenon to describe both both undercutting and melting of bulk silicon. In addition, undercutting occurs only after the top layer has been ablated away. Referring to Figure 4-14, at 10 pulses, there is no undercutting while undercutting begins to take place after 15 pulses. At 10 pulses, the top layer of silicon does not follow the profile of the beam. This indicates that the undercutting is not caused by the intensity distribution of the beam. Instead, it may be caused by reflection. The reflection may come from any number of surfaces, such as the liquid or amorphized bulk Si. Liquid silicon has a much higher reflectivity than c-Si. The bubble in the SiO_2 can also reflect much of the beam and cause undercutting.

Chapter 6

Conclusions and Future Work

To summarize, we have observed amorphous silicon after fs laser ablation. Although it has been hypothesized that amorphization occurs below the ablation threshold, this is the first time it has been directly observed. The lips around the hole indicate that the material is molten and could be pushed above the surface. This indicates that femtosecond ablation still involves thermal effects.

The laser effect can extend past the surface and modify the bulk silicon. There are many results of this interaction, namely the melting of the bulk silicon, the creation of a bubble in the oxide, and the undercutting of the top layer.

FIB is a good technique for making cross-sectional TEM samples. With new features, such as an auto-FIB program with a micromanipulator, it may be possible to make cross-sectional TEM samples quicker than before. One does have to be cautions of the thickness of the sample and the amount of amorphous damage.

Femtosecond lasers have contributed greatly to laser machining in making features with small heat affected zones. This makes it suitable for delicate work. However, as technology pushes for smaller and smaller features, the heat affected zone will eventually have to be taken into consideration.

For future work, a one dimensional simulation for melting and solidification would be useful. Since the beam diameter is greater than the absorption depth, lateral heat diffusion

can be neglected, So the phenomenon can be accurately modeled in one-dimension [25].

To further investigate the bulk effects, it would be useful to run a few experiments with a 1 μm thick oxide. If the bulk is within the spread of the focal point, increasing the distance between the bulk and the surface should eliminate any interaction. We could then further investigate the evolution of the bulk Si, the bubble, and the undercutting.

The more readily amorphized <111> plane can be investigated with this TEM methodology to investigate the thickness of the amorphized region. It would also be useful to distinguish if ablation occurs via particle expulsion or via a vapor plume.

Appendix A

Measurement of Laser Parameters

A.1 Introduction

Calculations will be performed in this appendix for the various laser parameters, such as the spot size, the intensity of the laser beam, and the focal depth. We will also discuss the focusing of the laser beam.

A.2 Laser Spot Size

For this section, please refer to figure A-1. The calculation of the laser spot size, s, after the 2.5 mm lens, was made using the equation

$$s = 2.44 \times f\# \times \lambda \tag{A.1}$$

where λ is the wavelength of the laser and f# is defined as

$$f\# = \frac{f}{d} \tag{A.2}$$

where f is the focal distance and d is the diameter of the entrance pupil of the lens. This relationship is valid only for a Gaussian beam. Through the geometry for the lens, we also

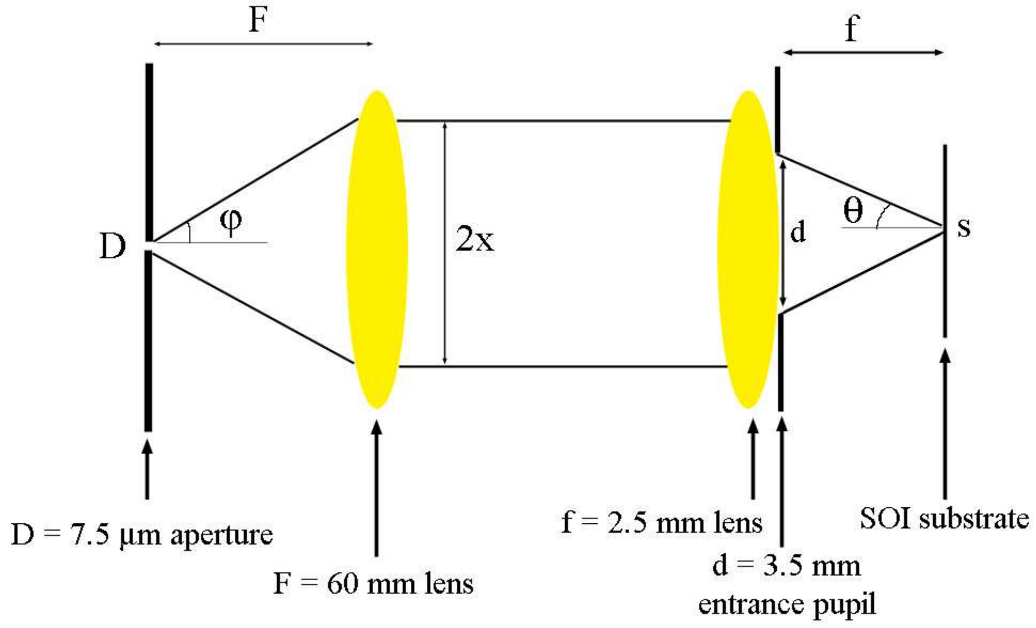

Figure A-1: A schematic diagram of the last two lenses in the laser setup.

know that

$$tan\ \theta = \frac{d}{2f} \tag{A.3}$$

so that

$$f\# = \frac{1}{2tan\ \theta}. \tag{A.4}$$

Since the numerical aperture (NA) is given by

$$NA = sin\ \theta \tag{A.5}$$

and our NA = 0.55. Our spot size is calculated to be

$$s = 478\ nm. \tag{A.6}$$

A.3 Intensity of the Laser Beam

For this section, please refer to figure A-1. The energy of the laser beam is Gaussian which is of the form

$$f(r) = I_0 exp\left[-\frac{r^2}{\sigma^2}\right](2\pi r), \tag{A.7}$$

where σ is related to the full-width-half-max (FWHM). The FWHM is also the spot-size, s, calculated in equation A.6. The FWHM and σ are related by

$$FWHM = 2\sqrt{2ln2}\sigma, \tag{A.8}$$

thus

$$\sigma = 201\ nm. \tag{A.9}$$

I_0 cannot be directly measured since the intensity of the beam is too low at the silicon surface. Furthermore, the NA is very high, causing the beam to diverge quickly, making it difficult to collect the beam for measurement. However, the intensity can be measured before the 2.5 mm lens, and I_0 is related to the percentage of energy transmitted through the lens.

There are two points for loss of beam intensity before and after the lens. The entrance pupil only allows a percentage of the beam to enter the lens. Then, only a fraction of the beam will be transmitted through to the substrate. To find the percentage of energy transmitted through the final lens, we need to find the diameter of the laser beam before the lens. We find x using the relationship

$$\varphi = 1.22\frac{\lambda}{D}, \tag{A.10}$$

where D is the diameter of the hole in the aperture. Through geometry, we know that

$$tan\ \varphi = \frac{x}{F} \sim \varphi, \tag{A.11}$$

where F is the focal distance. For our setup, $\lambda = 258$ nm, D = 7.5 μm, F = 60 mm so that the beam diameter is

$$2x = 4.4\ mm. \tag{A.12}$$

The entrance pupil on the final lens, d = 3.5 mm, is smaller than the incoming beam. The percentage of energy that enters the lens is the square of the ratio between the beam width and the diameter of the entrance pupil.

To find the percentage transmitted through the lens, we referenced the manufacturer's specification. Please refer to the Mitutoyo catalogue for the (UV80X, f = 2.5 mm, N.A. = 0.55) lens. At $\lambda = 258$ nm, ~50% of the laser beam will be transmitted through the lens. This gives us a total throughput of the lens is

$$\left(\frac{3.5}{4.4}\right)^2 \times 50\% = 31\%. \tag{A.13}$$

Now that we know the throughput, we need to measure the average intensity for the 4.4 mm spot. This was measured to be 0.42 ± 0.21 nJ/pulse·cm^2. This means that 0.13 ± .065 nJ/pulse·cm^2 is transmitted through the final lens. Since

$$I_{ave} = \int_0^{\frac{FWHM}{2}} f(r)dr \tag{A.14}$$

we can calculate I_0 from this measurement,

$$I_0 = (7.013 \pm 3.51) \times 10^7 nJ/pulse \cdot cm^2. \tag{A.15}$$

A.4 Focal Depth

For a schematic diagram of the focal depth, please refer to figure 5-1. The focal depth (FD) is the range over which the laser is at its peak intensity. To find the focal depth, use the equation

$$FD = \frac{\pi\sigma_1^2}{\lambda}, \tag{A.16}$$

where

$$\sigma_1 = \frac{s}{2}. \quad (A.17)$$

The spot size, s, is calculated in the previous section and the $\lambda = 258$ nm. Thus the focal depth is

$$FD = 997\ nm. \quad (A.18)$$

A.5 Finding the Focus Distance of the Laser Beam

After mounting the sample onto the XYZ stage, we first made sure the sample was flat by adjusting the tip and tilt. Rough focusing was done live with the video camera. After that, we used the laser to find the optimal position for drilling. The piezoelectric stage was stepped through the z axis by 0.5 μm. At each z, a row of 5 holes were drilled. The z which corresponded to the "best" drilled holes was used for drilling the sample. Figure A-2 is an SEM image of an array of holes that were scanned through several micrometers in the z direction.

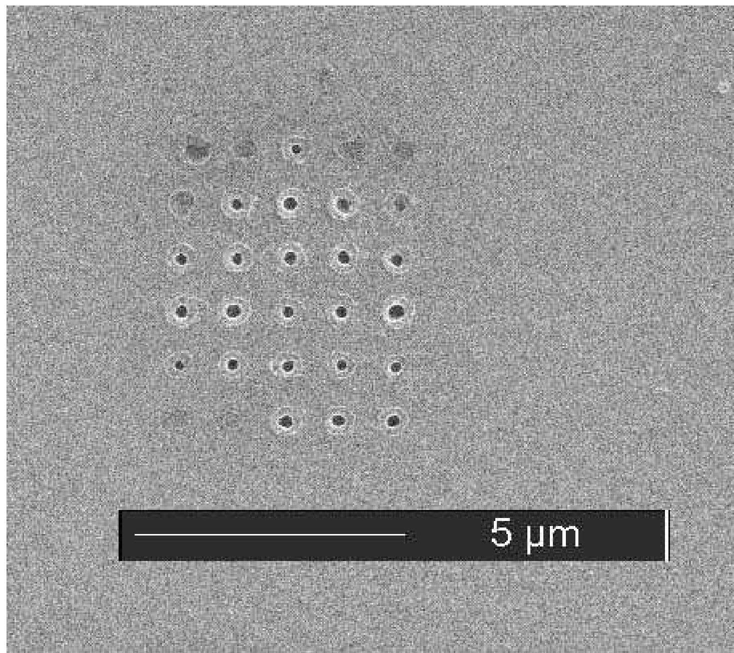

Figure A-2: An array of holes made to find the focus point. The row with the best holes represented the optimal focal distance.

Appendix B

TEM Sample Preparation

The substrate was a square piece of silicon 3 × 3 mm in size. A 200 μm cross, as seen in Figure B-1 was drilled to facilitate location of the feature subsequent in processing steps. The analyzed holes were drilled near the intersection. We begin with coating with metals. Then we discuss die-saw techniques and end with FIB techniques.

B.1 Coating with Metal

The preparation of TEM samples using FIB is a common process and protecting the sample from the ion beam is crucial in obtaining valid results. The sample must be protected from side wall damage as well as surface damage. Amorphization on the side walls can be significant [26]. The side wall damage was limited to 40 nm on each side by using lower beam currents for the final cuts. Initial cuts were made at 20 kpA and the final cuts were done at 100 pA. The minimum thickness of our sample was 120 nm in order to assure that at least 40 nm of crystalline material was sandwiched between two amorphous layers.

It was necessary to deposit both a chromium and a platinum layer before using the FIB to protect the top surface. This is because ion beam assisted CVD in the FIB may damage our features which are located on the surface. The density of the metal determines how sharp an edge will be milled. Low density metals, such as chromium, trap stray ions not above a

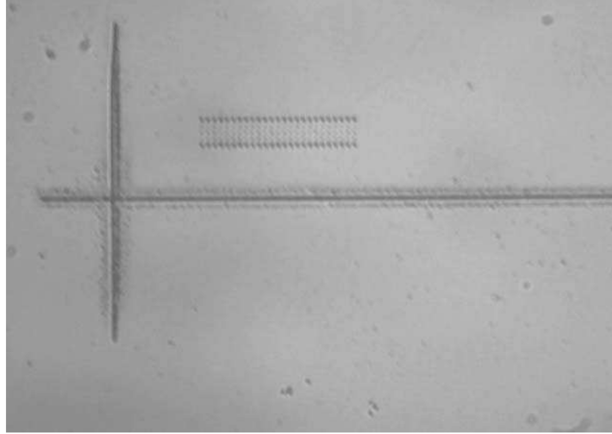

Figure B-1: Drilled area and the cross hair.

milling threshold which allows for good edge definitions. Figure B-2 is a chrome mask after FIB milling. However, some trapped ions may penetrate the metal and amorphize the silicon underneath. High density metals, such as platinum (Pt), prevent ion penetration, forcing oversprayed ions to mill away surface atoms. This results in a much shorter lifespan for the mask as it is constantly being worn away by oversprayed ions and results in a rounded edge. Figure B-3 shows a platinum mask after FIB milling. Using a combination both Pt and Cr allows for protection of the surface from the ion beam and for sharp edge definition. Since Cr is used as an adhesion layer for Pt, our final mask was a sandwich structure of Cr/Pt/Cr. Figure B-4 is a 35 kX SEM of the edge of the trench after FIB milling. The milling definition is very sharp. In this micrograph, it is possible to see the layers of the SOI structure as well.

B.2 Die-Saw Technique

The challenge here was to cut out a 200-300 μm sliver without losing it in the machine. We mounted the $3 \times$ 3 mm silicon sample onto a 4" wafer with crystal bond, a clear, silica-based gel. The sample was completely covered with the gel. Using the eyepiece on the die-saw, we then located the feature and cut 200-300 μm around it. The sample was placed in acetone which dissolves the crystal bond in order to unmount the slivers. This was successful about

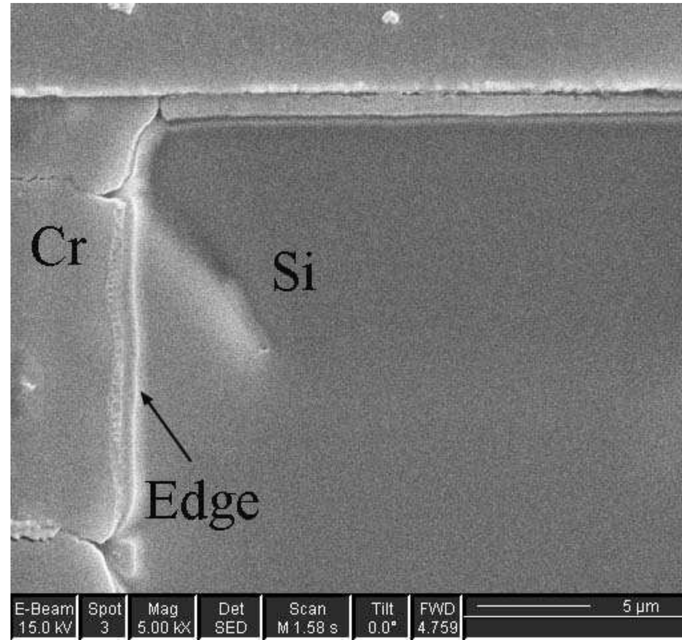

Figure B-2: FIB milled edge of a sample masked with Cr. Note the well defined edge.

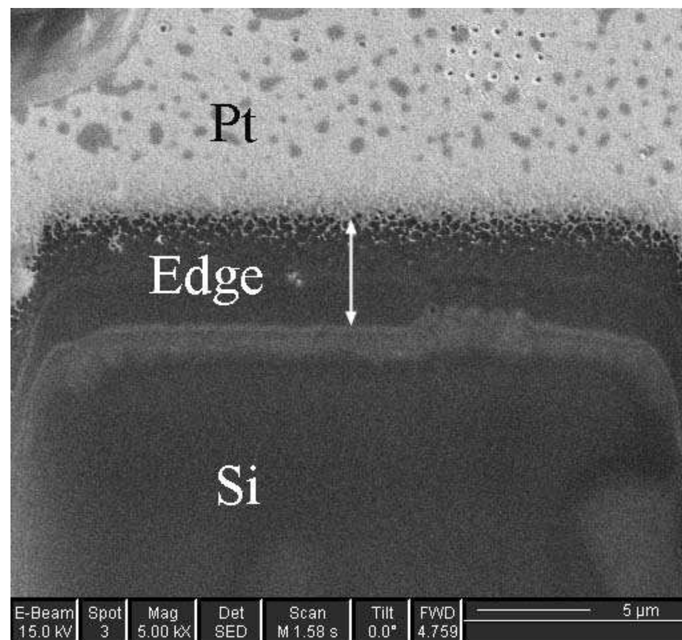

Figure B-3: FIB milled edge of a Platinum masked sample. Note the large overspray due to the ion beam.

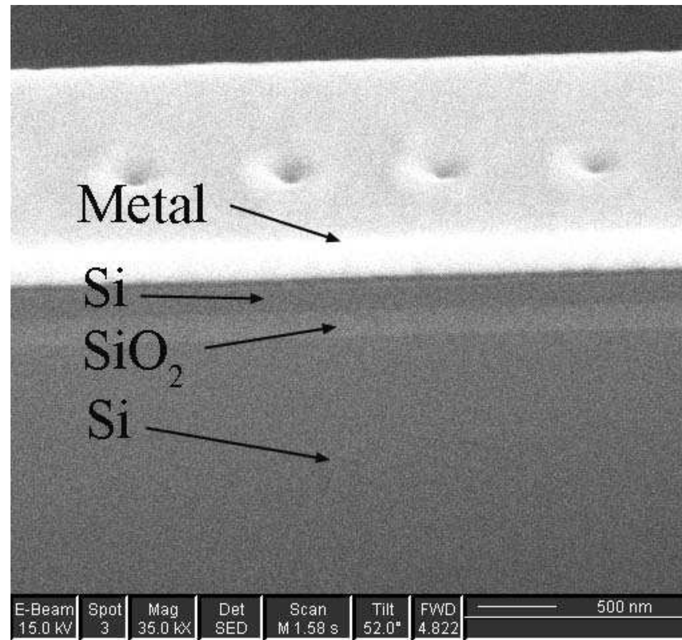

Figure B-4: Note the good edge and protection with a sandwich mask of Cr/Pt/Cr.

50% of the time. Figure B-5 is an optical micrograph of the sliver.

B.3 FIB Technique

The AutoFIB program available on the FIB only mills samples down to 700 nm. This was not thin enough for our purposes, so milling was done manually.

First, rough cuts at 20 kpA were made that were 30 nm wide and went from the edge of the sliver to 15 μm away from the holes (Figure B-6). The trench was milled to a depth greater than 2 μm. Ion beam current of 3 kA was used to mill the sample to 2 μm from the holes (Figure B-7). Both of these used the "square" rough cuts feature. The rotation of the sample had to be well controlled in order for the sample to cut through all the holes in all the cuts. Then the 100 pA beam in fine "rastering" mode was used (Figure B-8). At this point, it was crucial to use the SEM concurrently to observe the milling progress. After every two or three cuts, a SEM picture was taken. Since the holes were filled with metal, it was easy to see if a cross section was attained by observing the metal in the hole. When

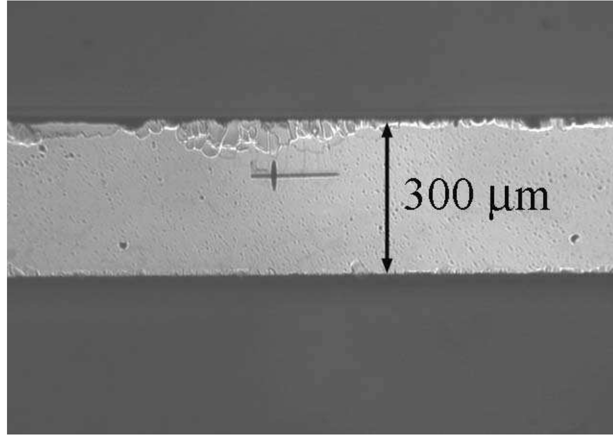

Figure B-5: Optical microscope picture of a 300 μm wide sliver.

that point was reached, the sample was turned around and the same process was repeated on the other side. This assured that we would be analyzing the cross section of the holes with no silicon bulk in the way. Figure B-9 shows an SEM image of a sample after the final milling. On the right, there is the array of holes, and the trench is milled to cut through the holes.

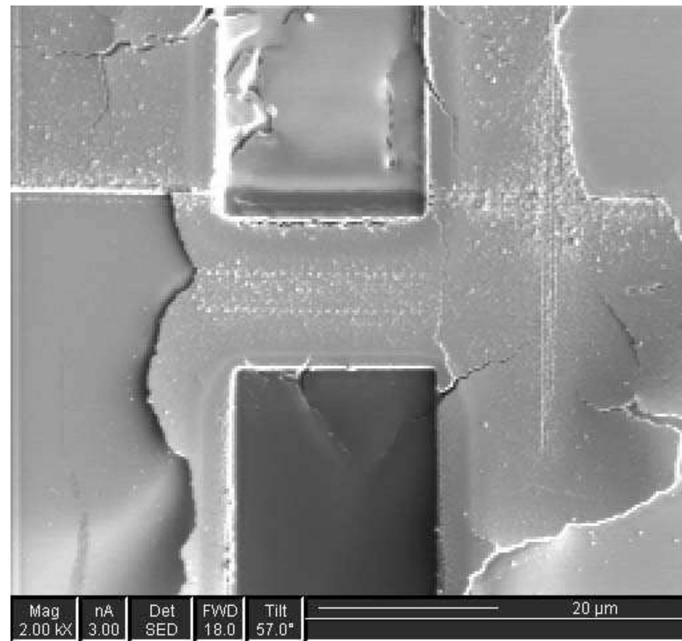

Figure B-6: After a 20 kpA rough milling in the FIB

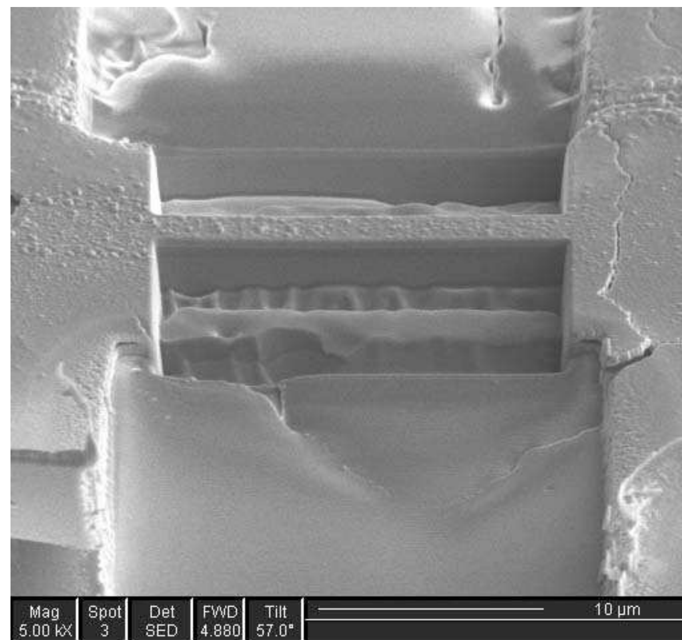

Figure B-7: After the 2nd milling with a 3 kpA beam

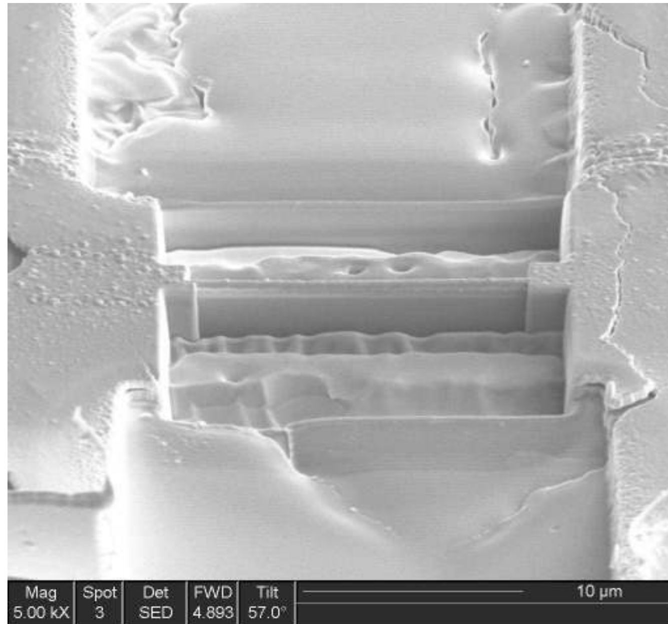

Figure B-8: After 100 pA fine milling.

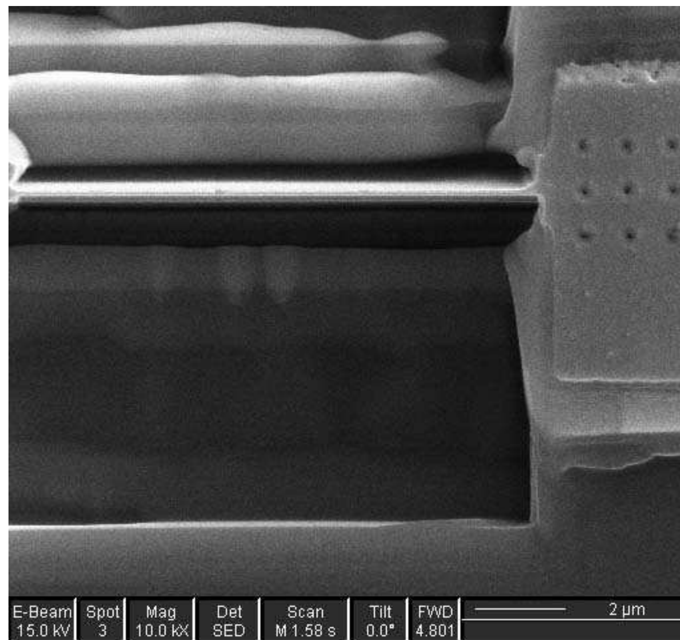

Figure B-9: Top view of the milled sample. Note the three rows of alignment holes on the right. The middle row is the row with the drilled samples.

Bibliography

[1] X. Liu, D. Du, and G. Mourou, *IEEE J. Quant. Elec.* **33**, 1706 (1997).

[2] N. M. Bulgakova, and I. M. Bourakov, *Appl. Surf. Sci.* **197-198**, 197 (2002).

[3] B. N. Chichkov, C. Momma, S. Nolte, F. von Alvensleben, and A. Tünnermann, *Appl. Phys. A* **63**, 109 (1996).

[4] M. Li, K. Mori, M. Ishizuka, and X. Liu, *Appl. Phys. Lett.* **83**, 216 (2003).

[5] K. Venkatakrishnan, B. Tan, and N. R. Sivakumar, *Optics & Laser Tech.* **34**, 575 (2002).

[6] R. Le Harzic, N. Huot, E. Audouard, C. Jonin, and P. Laporte, *Appl. Phys. Lett.* **80**, 3886 (2002).

[7] M. Ye, and C. P. Grigoropoulos, *J. of Appl. Phys.* **89**, 5183 (2001).

[8] A. Borowiec, M. Mackenzie, G.C. Weatherly, and H.K. Haugen, *Appl. Phys. A* **76**, 201 (2003).

[9] J. Bonse, S. Baudach, J. Krüger, W. Kautek, and M. Lenzner, *Appl. Phys. A* **74**, 19 (2002).

[10] M.C. Downer, R.L. Fork, and C.V. Shank, *J. of the Opt. Soc. of Amer. B* **2**, 595 (1985).

[11] A. Cavalleri, K. Sokolowski-Tinten, J. Bialkowski, and M. Schreiner, D. von der Linde, *J. of Appl. Phys.* **85**, 3301 (1999).

[12] P.P. Pronko, S.K. Dutta, J. Squier, J. V. Rudd, D. Du, and G. Mourou, *Opt. Comm.* **114**, 106 (1995).

[13] T. Q. Jia, Z. Z. Xu, X. X. Li, R. X. Li, B. Shuai, and F. L. Zhao, *Appl. Phys. Lett.* **82**, 4382 (2003).

[14] J. Bonse, J. M. Wrobel, J. Krüger, and W. Kautek, *Appl. Phys. A* **72**, 89 (2001).

[15] G. Dumitru, V. Romano, H. P. Weber, M. Sentis, and W. Marine, *Appl. Phys. A* **74**, 729 (2002).

[16] P. M. Fauchet, *Phys. Lett.* **93A**, 155 (1983).

[17] T. V. Kononenko, V. I. Konov, S. V. Garnov, R. Danielius, A. Piskarskas, G. Tamoshauskas, and F. Dausinger, *Quantum Elec.* **29**, 724 (1999).

[18] P. L. Liu, R. Yen, N. Bloembergen, and R. T. Hodgson, *Appl. Phys. Lett.* **34**, 864 (1979).

[19] D. Perez, and L. J. Lewis, *Phys. Rev. Lett.* **89**, 255504 (2002).

[20] H. Kurz, *Materials Research Society Symposia Proceedings* **74**, 3 (1986).

[21] Y. Hirayama, and M. Obara, *Appl. Surf. Sci.* **197-198**, 741 (2002).

[22] J. A. Yater, and M. O. Thompson, *Phys. Rev. Lett.* **63**, 2088 (1989).

[23] J. A. Van Vechten, R. Tsu, F. W. Saris, and D. Hoonhout, *Phys. Lett.* **74A**, 417 (1979).

[24] J. A. Van Vechten, R. Tsu, F. and W. Saris, *Phys. Lett.* **74A**, 422 (1979).

[25] K. Sokolowski-Tinten, J. Bialkowski, and M. Boing, *Phys. Rev. B* **58**, 805 (1998).

[26] J. P. McCaffrey, M. W. Phaneuf, and L. D. Madsen, *Ultramicroscopy* **87**, 97 (2001).

[27] K. Sokolowski-Tinten, J. Bialkowski, A. Cavalleri, and D. von der Linde, *Phys. Rev. Lett.* **81**, 224 (1998).

[28] E.P. Donovan, F. Spaepen, D. Turnbull, J. M. Poate, and D. C. Jacobson, *Appl. Phys. Lett.* **42**, 698 (1983).

[29] J. M. Liu, R. Yen, H. Kurz, and N. Bloembergen, *Appl. Phys. Lett.* **39**, 755 (1981).

[30] P. Simon, and J. Ihlemann, *Appl. Phys. A* **63**, 505 (1996).

[31] M. O. Thompson, J. W. Mayer, A. G. Cullis, H. C. Webber, N. G. Chew, J. M. Poate, and D. C. Jacobson, *Phys. Rev. Lett.* **50**, 896 (1983).

[32] R. F. Wood, and G. E. Giles, *Phys. Rev. B* **23**, 2929 (1981).

[33] D.R. Lide, Ed., *CRC Handbook of Chemistry and Physics,* CRC Press, Boca Raton (1992)

[34] P. Schvan and R. E. Thomas, *J. Appl. Phys* **10**, 4738 (1985).

[35] Y. S. Sung, H. Takeya, K. Hirata, and K. Togano, *Appl. Phys. Lett.* **83**, 1122 (2003).

[36] A. Luft, U. Franz, A. Emsermann, and J. Kaspar, *Appl. Phys. A* **63**, 93 (1996).

[37] M. Lenzner, J. Krüger, S. Sartania, Z. Cheng, Ch. Spielmann, G. Mourou, W. Kautek, and F. Krausz, *Phys. Rev. Lett.* **80**, 4076 (1998).

[38] B.C. Stuart, M. D. Feit, A. M. Rubenchik, B. W. Shore, and M. D. Perry, *Phys. Rev. Lett.* **74**, 2248 (1995).

[39] M. Li, M. Ishizuka, X. Liu, Y. Sugimoto, N. Ikeda, and K. Asakawa, *Opt. Comm.* **212**, 159 (2002).

[40] K. Nagayama, K. Suizu, and N. Zaima, *Appl. Phys. A* **69** **[Suppl.]**, S707 (1999).

[41] R.F.W. Herrmann, J. Gerlach, and E.E.B. Campbell, *Appl. Phys. A* **66**, 35 (1998).

[42] X. Mao, S. S. Mao, and R. E. Russo, *Appl. Phys. Lett.* **82**, 697 (2003).

[43] B. Angleraud, J. Aubreton, and A. Catherinot, *Eur. Phys. J. AP* **5**, 303 (1999).

[44] D. H. Lowndes, J. D. Fowlkes, and A. J. Pedraza, *Appl. Surf. Sci.* **154-155**, 647 (2000).

[45] J. M. Liu, *Opt. Lett.* **7**, 196 (1982).

[46] S. Ameer-Beg, W. Perrie, S. Rathbone, J. Wright, W. Weaver, and H. Champoux, *Appl. Surf. Sci.* **127-129**, 875 (1998).

[47] J. Békési, J.-H. Klein-Wiele, and P. Simon, *Appl. Phys. Lett.* **76**, 355 (2003).

[48] I. Zergioti, S. Mailis, N. A. Vainos, C. Fotakis, S. Chen, and C. P. Grigoropoulos, *Appl. Surf. Sci.* **127-129**, 601 (1998).

[49] A. Semerok, B. Sallé, J.-f. Wagner, and G. Petite, *Laser and Part. Beams* **20**, 67 (2002).

[50] E. G. Gamaly, A. V. Rode, and B. Luther-Davies, *Phys. of Plasmas* **9**, 949 (2002).

[51] R. E. Russo, X. Mao, J. J. Gonzales, and S. S. Mao, *J. Anal. At. Spectrom.* **17**, 1072 (2002).

[52] S. Amoruso, X. Wang, C. Altucci, C. De Lisio, M. Armenante, and R. Bruzzese, *Appl. Phys. Lett.* **77**, 3728 (2000).

[53] K. Dou, E. T. Knobbe, R. L. Parkhill, B. Irwin, L. Matthews, and K. H. Church, *Appl. Phys. A* **76**, 303 (2003).

[54] B. Sallé, O. Gobert, P. Meynadier, M. Perdrix, G. Petite, and A. Semerok, *Appl. Phys. A* **69**, S381 (1999).

[55] L. Saraf, C. Wang, M. H. Engelhard, and D. R. Baer, *Appl. Phys. Lett.* **82**, 2230 (2003).

[56] S. Nakahara, *Surf. & Coat. Tech.* **169-170**, 721 (2003).

[57] C.Z. Wang and K.M. Ho, *Surf. Rev. and Lett* **6**, 1025 (1999).

[58] M. O. Thompson, G. J. Galvin, J. W. Mayer, P. S. Peercy, J. M. Poate, D. C. Jacobson, A. G. Cullis, and N. G. Chew, *Phys. Rev. Lett.* **52**, 2360 (1984).

[59] A. Kokorowski, G. L. Olson, J. A. Roth, and L. D. Hess, *Phys. Rev. Lett.* **48**, 498 (1982).

[60] M. G. Grimaldi, P. Baeri, and M. A. Malvezzi, *Phys. Rev. B* **44**, 1546 (1991).